Continental Shelf Research 46 (2012) 31–49

Contents lists available at SciVerse ScienceDirect

Continental Shelf Research

journal homepage: www.elsevier.com/locate/csr

On the vertical and temporal structure of flow and stress within the turbulent oscillatory boundary layer above evolving sand ripples

Alex E. Hay [a,*], Len Zedel [b], Richard Cheel [a], Jeremy Dillon [b]

[a] Department of Oceanography, Dalhousie University, Canada B3H 4R2
[b] Department of Physics and Physical Oceanography, Memorial University of Newfoundland, Canada A1B 3X7

ARTICLE INFO

Article history:
Received 19 May 2011
Received in revised form
8 February 2012
Accepted 18 February 2012
Available online 7 March 2012

Keywords:
Turbulent oscillatory boundary layer
Shear stress
Sand ripple
Friction factor
Coherent Doppler profiler
Multi-frequency

ABSTRACT

The vertical structure of flow and stress within turbulent oscillatory boundary layers above evolving sand ripples is investigated in experiments carried out using a prototype wide-band coherent Doppler profiler in an oscillating boundary facility with beds of 0.216 mm median diameter sand, 10 s oscillation period, and 0.9 m excursion (Shields parameter = 0.11). The bed evolved from an initial nominally flat state through 5 cm wavelength, nearly two-dimensional ripples to 12 cm wavelength, three-dimensional ripples. Average ripple height increased from 0.2 cm to 1.4 cm, corresponding to roughness Reynolds numbers between 68 and 7700. Average ripple steepness increased from 0.03 to 0.15. Bed elevation spectra exhibit the shift towards lower spatial frequencies observed by Davis et al. (2004) and, at higher spatial frequencies, a saturation range analogous to that in surface gravity wave spectra. Horizontal velocity profiles exhibit the phase lead and overshoot expected for oscillatory boundary layer flow. Bottom stress estimates are obtained from the acceleration defect, the Reynolds stress and the law-of-the-wall. The defect stress estimates are bounded above and below by the Reynolds stress and the law-of-the-wall estimates, respectively. The values of the bottom friction coefficient and hydraulic roughness from the defect stress estimates are consistent with results from previous work on equilibrium orbital-scale ripples, as summarized by Nielsen (1992), indicating that ripple evolution was quasi-steady.

1. Introduction

This is the third in a series of papers treating observations of the vertical structure of turbulent oscillatory boundary layers above hydrodynamically rough surfaces. The first and second papers deal with the boundary layer above fixed roughness beds, the first of the two investigating the vertical structure of the horizontal velocity (Hay et al., 2012a), the second turbulence and stress (Hay et al., 2012b). This third paper presents results from an additional set of experiments using a bed of mobile sand, the surface of which evolved from an initially flattened state through two- and three-dimensional ripples over the time course of each experiment. The flow measurements reported in all three papers were made with a prototype wide-band coherent Doppler profiler developed for studying the fluxes of momentum and sediment in the bottom boundary layer under both waves alone and combined wave-current forcing. The principal motivation for developing this new instrument, the MFDop, is the longstanding lack of suitable technologies for measuring stress and sediment dynamics under such conditions without disturbing either the mobile bed or the near-bed flow (Grant and Madsen, 1986).

In the more than two decades following Grant and Madsen's (1986) seminal review, substantial progress has been made towards obtaining field measurements of flow and turbulence within the wave bottom boundary layer. In some cases, advances have been made using invasive methods, notably a Laser Doppler Velocimeter (LDA) mounted on a mechanical stage to obtain vertical profiles point-by-point (Trowbridge and Agrawal, 1995), and a vertical stack of hot-film anemometers spanning the boundary layer and inserted into the bed (Foster et al., 2000). However, both of these approaches have significant limitations, with the result that non-invasive methods have been and continue to be actively pursued. Pulse-coherent acoustic Doppler sonar offers considerable potential in this application, providing a measurement which, rather than being at a single point, is acquired essentially instantaneously along an intrinsically bottom-referenced profile from a location distant from the bed. The technology also functions well in, and indeed is improved by, conditions of high suspended sediment concentration, conditions which can be limiting for systems based on optical techniques. The advantage of pulse-coherent Doppler over other Doppler velocity estimation methods is its comparatively higher accuracy

* Corresponding author. Tel.: +1 902 494 6657; fax: +1 902 494 3877.
E-mail address: Alex.Hay@Dal.Ca (A.E. Hay).

0278-4343/$ - see front matter © 2012 Elsevier Ltd. All rights reserved.
doi:10.1016/j.csr.2012.02.009

at high range resolution. However, because the velocity estimates are based on pulse-to-pulse variations in the phase of the signal, ambiguous velocities result if the actual phase change due to scatterer motion extends beyond $\pm\pi$. Depending on the application, it may be possible to operate within the unambiguous range (Lhermitte and Lemmin, 1994). Under energetic wave conditions in shallow water, however, phase wraps associated with the wave-current and the turbulent velocities are likely to occur both frequently and irregularly. In our earlier implementations of the technique for nearshore dynamics studies (e.g. Smyth et al., 2002), use was made of the fact that the velocity goes to zero at the bed to identify and remove the phase wraps during post-processing, a time-consuming and tedious process.

The central idea underpinning the MFDop design, as outlined in Hay et al. (2008), was to operate at multiple frequencies so as to make use of the frequency-dependence of the phase change to resolve the velocity ambiguities automatically (Zedel and Hay, 2010), and also to utilize the variation in backscatter amplitude with frequency to estimate suspended particle concentration and size. The use of dual pulse intervals in single-frequency operation is an alternative disambiguation method (Holleman and Beekhuis, 2003) but, compared to the multi-frequency approach, has the disadvantages that (a) the effective sampling rate is lower; and (b) the narrow frequency band of the signal contains little information on the size/concentration ambiguity in the scatterer population.

As summarized in Hay et al. (2012a), the development during the past two decades of coherent Doppler profilers for boundary layer studies in aqueous environments has been pursued by research groups worldwide. Profiling pulse-coherent Doppler systems are also available commercially but, notably, those suitable for use in field conditions tend to incorporate diverging monostatic beam geometries. In contrast, many of the prototype systems developed for research purposes (Stanton, 1996; Rolland and Lemmin, 1997; Hurther and Lemmin, 2001; Smyth et al., 2002; Betteridge et al., 2005) have opted for bistatic geometries to avoid the issues associated with estimating Cartesian velocity components from spatially separated radial velocities, issues which are especially problematic for flow over boundaries with high geometric roughness. The development of these research systems is ongoing, the MFDop representing one example. Hurther et al. (2011) have also implemented a multi-frequency capability, though for the purpose of Doppler noise reduction and particle size/concentration measurements: velocity ambiguities are resolved via time-domain changes in the Doppler shift at a single frequency.

The purpose of this paper is to present results from a set of experiments with the MFDop above evolving sand ripples, building on the fixed roughness experiments reported in Hay et al. (2012a, 2012b). Three main results were obtained from the fixed roughness studies. The first was that, for nominally flat beds of 370 μm diameter sand and 4 mm diameter gravel, the closest to the bed that velocity measurements could be made was 5 ± 1 mm. This conclusion was reached on the basis of: (a) the maximum bedward extent of the logarithmic region of the velocity profile; and (b) the phase and magnitude of the horizontal velocity profiles measured with the MFDop compared to the LDA measurements reported by Sleath (1987) and Jensen (1988). The second main result was that estimates of bottom stress obtained with the MFDop were in satisfactory agreement with the wave friction factor relation proposed by Nielsen (1992) (which is a modification of the earlier relation of Swart (1974) accounting for later measurements). The third main result was that this agreement was obtained only for stress estimates based on the vertical integral of the momentum equation: estimates via the Reynolds stress and the law-of-the-wall methods were respectively low and high. Given that redundant measures of stress are highly desirable, as Grant and Madsen (1986) were careful to point out, this lack of consistency among independent stress estimates is disappointing. However, similar inconsistencies were reported for the LDA-based measurements over rough beds, with Sleath (1987) concluding that the momentum integral approach was best, while Jensen et al. (1989) favoured the law-of-the-wall. Thus, there are questions outstanding as to the most suitable/reliable stress estimation technique(s) in turbulent oscillatory flows.

As indicated in the opening paragraph, the purpose of this paper is to present the results of our measurements of flow and turbulence within the oscillatory boundary layer above beds of evolving sand ripples. The development of ripples from an initially flat bed has a long history, with the study by Bagnold (1946) on equilibrium orbital ripple height and wavelength laying the groundwork for subsequent laboratory investigations of the bottom stress associated with equilibrium orbital-scale ripples (Carstens et al., 1969; Lofquist, 1986). A focus of more recent studies has been the time history of ripple development: in the laboratory (Davis et al., 2004; Smith and Sleath, 2005; Testik et al., 2005); in the field (Traykovski, 2007; Maier and Hay, 2009; Hay, 2011); and in numerical models (Marieu et al., 2008; Chou and Fringer, 2010). To our knowledge, however, there has been no previous study in which bottom stress, which is the forcing mechanism responsible for mobile bed adjustment, has been measured as the bed evolves.

Thus, the present paper addresses the following questions. (1) Can representative measurements of velocity and stress over sand ripples evolving under oscillatory flow be obtained with the MFDop? (2) Are the estimates of stress obtained over evolving ripples via the law-of-the-wall, the Reynolds stress, and the vertically integrated momentum equation, comparable? (3) How does bottom stress change with ripple height, wavelength and steepness as the bed evolves? (4) How do these dependencies of stress on ripple geometry for evolving ripples compare to existing relationships based on equilibrium ripples?

The paper is organized as follows. The relevant aspects of oscillatory boundary layer theory are summarized in Section 2, and the methods in Section 3. The results are presented in Section 4 including: the evolution of ripple properties with elapsed time after test initiation; the phase-averaged horizontal velocity including vertical profiles of magnitude and phase; the stress estimates; the variation of friction velocity with RMS bed elevation; and the variation of the bottom friction factor and hydraulic roughness with ripple geometric roughness. Section 5 is a discussion. The conclusions of the study are presented in Section 6.

2. Theory

The momentum equation for the boundary layer over a horizontal flat bed in oscillatory flow can be written (e.g. Batchelor, 1967; Fredsoe and Deigaard, 1992) as

$$\frac{\partial u}{\partial t}=\frac{1}{\rho}\frac{\partial \tau}{\partial z} \tag{1}$$

where x and z are the horizontal and vertical coordinates, ρ is the density of the fluid, τ is the shear stress, and u is the defect velocity

$$u=\hat{u}-\hat{u}_{\infty} \tag{2}$$

which appears via the boundary layer approximation (e.g. Batchelor, 1967), by which the pressure gradient term is eliminated from the momentum equation for the boundary layer.

In the case of the boundary layer above an oscillating flat plate with no imposed flow in the interior, Eqs. (1) and (2) again apply, but with $\hat{u}_\infty \equiv 0$ (Batchelor, 1967). Thus, the governing equations for the boundary layer above an oscillating boundary in an otherwise motionless fluid are mathematically equivalent to the equations governing the boundary layer over a stationary flat plate in oscillatory flow.

Analytical solutions to Eq. (1) can be obtained by adopting an eddy viscosity representation of the stress. A wide range of forms for the eddy viscosity have been proposed (see Justesen, 1988; Sleath, 1990a, for reviews). The models predict that the boundary layer flow leads the flow in the interior, and that the velocity magnitude within the boundary layer overshoots the amplitude of the oscillatory flow in the interior, though the predicted values for the maximum phase lead and overshoot vary among the models. The horizontal flow within the boundary layer can be written as

$$\hat{u}(t) = \hat{u}_0(z)\,\sin[\omega t + \hat{\phi}_0(z)] \tag{3}$$

where $\hat{u}_0(z)$ and $\hat{\phi}_0(z)$ are the amplitude and phase of the flow in the Eulerian reference frame fixed with respect to the bed, and ω is the angular frequency of the oscillation. Detailed measurements in turbulent oscillatory boundary layers above fixed roughness beds using LDA indicate values of 4–8% for the overshoot, and 20–30° for the maximum phase lead (Sleath, 1987; Jensen, 1988; Jensen et al., 1989). Our measurements with the MFDop over a fixed gravel bed yield comparable values (Hay et al., 2012a).

Oscillatory boundary layers are thin. The characteristic scale height, δ, can be estimated from Eq. (1) using the friction velocity u_* as the velocity scale, $\partial/\partial t = \omega$, and $\tau/\rho = u_*^2$ to obtain $\delta \sim u_*/\omega$. In the analytic models with time-invariant eddy viscosity, the scale height is (Christoffersen and Jonsson, 1985)

$$\delta = \kappa u_*/\omega \tag{4}$$

where $\kappa = 0.4$ is von Karman's constant. For the 5–20 s periods typical of wind-generated surface gravity waves in the ocean, ω is O(1) rad/s. Typical values of u_* are O(10) cm/s, so δ can be expected to be only a few cm. This thinness has been the major impediment to obtaining measurements of the vertical structure of flow and turbulence in the wave bottom boundary layer under field conditions, particularly above mobile beds.

In principle, the stress can be estimated using three independent methods: (1) the Reynolds stress; (2) the acceleration defect; and (3) the law-of-the-wall. The vertical turbulent flux of horizontal momentum is given by

$$\frac{\tau(z,t)}{\rho} = -\langle u'w' \rangle \tag{5}$$

where the primes denote the turbulent fluctuations, $\langle\ \rangle$ denotes a time or ensemble average, and $-\langle u'w' \rangle$ is the Reynolds stress. A second expression for the stress is obtained by vertically integrating the equation for the acceleration defect in the boundary layer: that is, from Eq. (1)

$$\frac{\tau(z,t)}{\rho} = -\int_z^\infty \frac{\partial u}{\partial t}\,\mathrm{d}z. \tag{6}$$

Because the r.h.s. of Eq. (6) is the vertical integral of the defect acceleration, the stress estimates obtained by this method are referred to here as the defect stress. The third method for determining the stress invokes the law-of-the-wall (e.g. Monin and Yaglom, 1971) which here takes the form

$$u(z,t) = \frac{u_*(t)}{\kappa}\,\ln(z/z_0) + u_K(t) \tag{7}$$

where u_K denotes the velocity of the moving boundary. The subscript K denotes the velocity of the RippleKart apparatus described in Section 3. Thus, at $z = z_0$, the height at which the no-slip condition is satisfied, u equals u_K rather than the usual value of zero.

In the above estimates, τ represents the total shear stress: that is, the vertical turbulent flux of horizontal momentum (Raupach, 1992). This quantity is a function of height above the bed, and over very rough boundaries issues arise, particularly when extrapolating shear stress measurements within the fluid to obtain the shear stress at the bed, as to the choice of z-origin, and of how best to take into account the fluid regions below the tops of the roughness elements when computing the spatially averaged stress (Raupach, 1992; Nikora et al., 2007). However, there is an additional non-trivial issue relating to the choice of z-origin for measurements of flow above mobile beds using Doppler sonar systems: the relative positions of the acoustically determined bed level and the hydrodynamic bed level. Thus, for example, the usual virtual origin $z = z' + \Delta$ in Eq. (7) associated with the zero-plane displacement height Δ (Monin and Yaglom, 1971) must now include an additional offset related to the likely non-zero difference between the hydrodynamic and acoustic bed levels. This point is taken up again in Sections 3.2, 4.3, and 5.5.

The bed friction factor in oscillatory flow, f_w, is defined by

$$u_{*m}^2 = \frac{f_w}{2} U_{0\infty}^2 \tag{8}$$

where $U_{0\infty}$ is the amplitude of the oscillatory motion in the interior and u_{*m} is the maximum value of the friction velocity during a half-cycle, i.e. $u_{*m} = \sqrt{\tau_{bm}/\rho}$, where τ_{bm} is the estimate of the half-cycle maximum stress at the bed. For the oscillating boundary configuration, $U_{0\infty}$ is replaced by the maximum speed of the boundary.

In previous studies of oscillatory boundary layers, it has been found that one or more of the three methods may yield unreliable estimates of stress. For example, Sleath (1987) found that the law-of-the-wall was of limited utility above beds of fixed sand, gravel and pebble bed roughness, while Jensen (1988) found that the defect method did not yield reliable stress estimates in his experiments with beds of fixed sand grains. All three methods are implemented here.

3. Methods

The experimental approach and methods closely follow those used in the earlier fixed roughness experiments, in part so that the estimates of various quantities and stress in particular are obtained in exactly the same way, except where indicated otherwise. Consequently, the methods are only briefly outlined here, and the reader is referred to Hay et al. (2012a, 2012b) for additional detail.

3.1. Experimental

The experiments were carried out in the RippleKart apparatus sketched in Fig. 1. The Kart is driven by a Scotch yoke assembly, which converts the rotary motion of the drive arm to rectilinear 10-s period nearly sinusoidal oscillations parallel to the long axis of the tank. (The idea for using a Scotch yoke drive mechanism came from Sleath (1990b), who used one in his studies of combined flow boundary layers.) The 10-cm thick bed of sand rests on a 2.4 m long $\times$ 0.8 m wide tray suspended beneath the Kart on thin stainless steel downriggers. Fared end pieces are mounted on each end of the tray, serving both to retain the sand and, via their fared shape, to minimize end effects on ripple development. The adjustable Kart excursion, d, was set at 90 cm for the experiments presented here. Commercially available

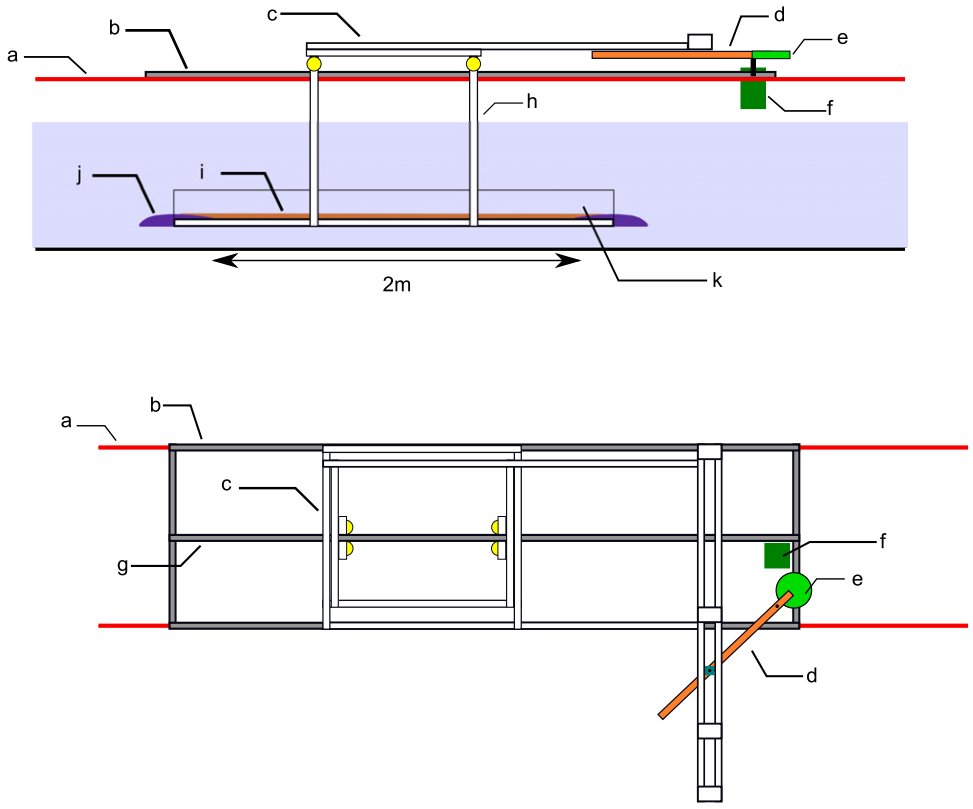

Fig. 1. RippleKart. Top panel, side view; bottom panel, top view: (a) top of tank sidewalls; (b) side rails; (c) Kart; (d) drive arm; (e) counterweight; (f) drive motor; (g) centre guide rail; (h) down-riggers; (i) sand bed; (j) fared end-pieces; (k) tray sidewalls. A drive belt (not shown) connects the motor to a pulley (not shown) centred on the axis of rotation of the drive arm. Water depth ca. 0.7 m; depth of sand–water interface ca. 0.5 m.

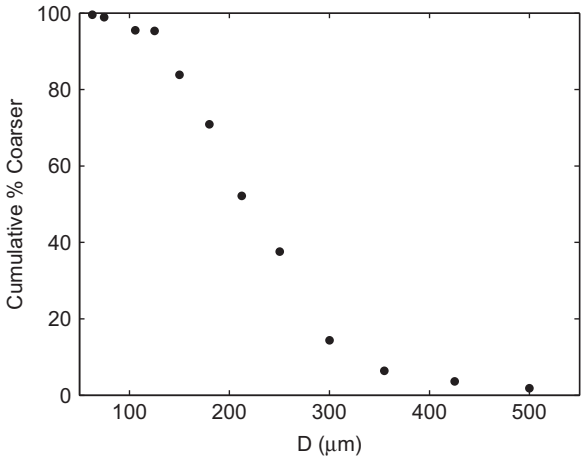

Fig. 2. Sand size distribution. The points represent cumulative % coarser than the indicated diameter, *D*.

quartz sand, marketed for sand blasting applications, was used in the experiments. The sand size distribution, determined by mechanically sieving the dry sand, is plotted in Fig. 2. The median size, D_{50}, was 216 μm. D_{16} and D_{84}, the 16% and 84% coarser than sizes, were 296 μm and 149 μm, respectively. The ratio $D_{84}/D_{16} \sim 2$ corresponds, according to Folk (1980), to moderately well-sorted to well-sorted sand.

Flow and turbulence above the bed were measured with the MFDop. This prototype wide-band pulse-coherent bistatic acoustic Doppler sonar operates in the ~1.2 to ~2.3 MHz frequency band. To evaluate the performance of the multi-frequency disambiguation method, simulations were run using the Doppler sonar model developed by Zedel (2008), resulting in optimization curves for disambiguous velocity range vs. frequency separation and noise level (Zedel and Hay, 2010). Independent tests of MFDop performance have been carried out in a turbulent wall jet (Hay et al., 2008), resulting in favourable comparisons to independent velocity measurements using a Nortek Vectrino. Also, favourable comparisons of velocity spectra extending into the inertial subrange were obtained in a turbulent round jet using Particle Image Velocimetry (PIV) as the independent velocity measurement (Dillon et al., 2011).

The MFDop transmits and receives up to four different frequencies simultaneously. The transmit signal is a digitally generated sinusoidal tone burst which starts and ends on a zero-crossing. In multi-frequency operation, phase is continuous at the transitions between successive frequencies in the multi-tone burst. The four frequencies can be chosen arbitrarily within the transducer bandwidth. The received signals are band-pass filtered and demodulated digitally. Programmable finite-impulse response (PFIR) filters are implemented in the digital down-converters. These filters set the passband for each frequency channel. The cutoff frequencies are defined, relative to the tone centre frequency, by the bandwidth corresponding to the duration of each tone. As in the fixed roughness experiments, the mobile bed tests were carried out with two PFIRs, each with a different impulse response.

The MFDop was operated in both single- and dual-frequency mode. In single-frequency operation, the full bandwidth of the transducers is exploited to achieve maximum range resolution, but ambiguity velocity wraps began to appear towards the later stages of the runs as ripple height and steepness increased. In dual-frequency operation, runs could be extended to longer times, but at half the range resolution. The MFDop operating parameters in both modes are listed in Table 1.

Table 1
MFDop operating parameters: the first set of values is for two-frequency operation; the second set for single-frequency operation.

Parameter	Dual	Single	Units
Frequency 1	1.6	1.7	MHz
Frequency 2	2.1	–	MHz
Pulse duration 1	2.0	1.18	μs
Pulse duration 2	2.05	–	μs
Pulse repetition interval	1.18	1.18	ms
Transmit amplitude	80	80	%
Receiver bandwidth	0.5	1	MHz
Pulse pairs per ensemble	10	10	
Ensemble acquisition rate	84.7	84.7	Hz
Range resolution 1	1.5	0.87	mm
Range resolution 2	1.54	–	mm
Range bin width	1.5	0.75	mm

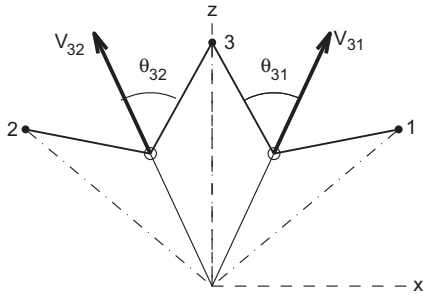

Fig. 3. Bistatic geometry. The solid circles indicate the transducer positions: 1 and 2 are the outboard, receive-only transducers; 3 is the transmit transducer. The angles θ_{31} and θ_{32} indicate the bisectors for each transducer pair. The measured velocities V_{31} and V_{32} are the projection of the Cartesian velocity vector $\vec{u}$ along these bisectors, as indicated. The open circles indicate the horizontally separated measurement points.

The MFDop transducer assembly consists of a centre transducer which both transmits and receives, and two outboard transducers operating in receive mode only (Fig. 3). The outboard transducers are symmetrically positioned in an isosceles bistatic geometry about the centre transducer. The angle between the emitter and receiver beam axes is 14°. The horizontal and vertical velocity components u and w are obtained from the projections of the flow velocity onto the unit vectors bisecting the beam intersections at each range cell for each of the two outboard/centre transducer pairs. In the isosceles geometry, the angle of the unit vector along the bisector, relative to the vertical, is equal for all range bins, and therefore the relative contributions of u and w to the measured (i.e. V_{31} and V_{32}) velocities are the same for all range bins (Hay et al., 2012a).

The MFDop was mounted beneath the centre guide rail (indicated by (g) in Fig. 1), and remained fixed as the Kart moved. The beam axis of the centre transducer was directed vertically downward, and the measurement plane (i.e. the plane containing the three beam axes) was aligned parallel to the long axis of the tank. In order to maintain sufficiently high signal strength during the experiments, agricultural lime (median diameter 21 μm) was added continuously from a mechanically stirred reservoir.

3.2. Analysis

The distance to the bed was determined using the backscatter amplitude from the vertical beam. The maximum amplitude was located within the 40–45 cm range interval spanning the bottom return, and the amplitude-weighted mean range, r_b, was determined using

$$r_b = \sum A_j r_j / \sum A_j \tag{9}$$

where the sum is over all range bins with amplitudes exceeding half the maximum. The mean range from the MFDop to the bed, $\overline{r}_b$, is the mean over the 10-s oscillation cycle of the phase-averaged values of $r_b(t)$. The phase average $\overline{\xi}(t_k)$ of some quantity ξ at time t_k during the oscillation cycle is given by

$$\overline{\xi}(t_k) = \frac{1}{N_c}\sum_{i=1}^{N_c} \xi(t_k + (i-1)T_K) \tag{10}$$

where N_c is the number of cycles included in the average, typically 13 (Table 2), and T_K is the Kart oscillation period. Following the notation used by Jensen et al. (1989), the overbar will denote phase-average throughout the remainder of the paper.

The amplitude, U_{K0}, and period, T_K, of the Kart motion were determined from a non-linear least-squares fit of $u(r_b,t)$ to a sinusoid, i.e. a fit to

$$u(r_b,t) = a \sin \omega t + b \cos \omega t \quad (\omega = 2\pi/T_K) \tag{11}$$

yielding best-fit values for T_K and U_{K0} (i.e. $[a^2+b^2]^{1/2}$). The time series data at each range were then interpolated onto a common time base at a sampling interval of $T_K/100$, and subdivided into individual cycles defined by successive zero up-crossings of the Kart velocity. The interpolation to a common time base defined by the Kart motion eliminated the (small) relative drift of the data acquisition computer clock and the synchronous AC motor driving the Kart. The values of T_K (mean ± standard deviation) for the different runs are listed in Table 2.

Table 2
RippleKart runs, mobile bed. Kart excursion, d=90.8 cm for all runs. Listed are the YearDay, YD, of each test; the run numbers (i.e. the data file extensions) for each test; water temperature, T; the programmable finite-impulse response digital filter, PFIR; the number of cycles used in the phase-averages out of a possible 13 maximum, N_c; the Kart oscillation period, T_K; and the full duration of each test.

YD	Runs	T (°C)	PFIR	N_c	T_K (s)	Duration (min)
242	000–015[a]	23	ICS[b]	13[c]	10.0008 ± 0.0019	45.7
245	000–015[a]	21.5	7-tap	13	10.0009 ± 0.0017	49.1
246	000–013[d]	21.5	7-tap	13	10.0007 ± 0.0021	40.8

[a] Dual-frequency.
[b] Manufacturer's default filter coefficients, 63-tap.
[c] Twelve for run 242.001.
[d] Single-frequency.

The range to the sediment–water interface was defined to be the range at which the gradient of the backscatter amplitude exceeded a specified threshold. This range was designated $\overline{R}_B(t_k)$, after low-pass filtering to remove quantization noise (10 Hz cutoff frequency). An example time series of phase-averaged backscatter amplitude is shown in Fig. 4, together with the corresponding time series of $\overline{r}_b(t_k)$ (white) and $\overline{R}_B(t_k)$ (black). The latter time series closely follows the edge which the mind's eye would choose for the sediment–water interface. $\overline{R}_B(t_k)$ was used to define the mean and minimum distance to the bed during the oscillation cycle, and therefrom the heights of the range cells above the bed, i.e.

$$z_j = \frac{1}{T_K}\int_0^{T_K} \overline{R}_B(t_k)\, dt_k - r_j \tag{12}$$

where r_j is the range from the centre transducer to the jth range bin. The height corresponding to the minimum distance to the

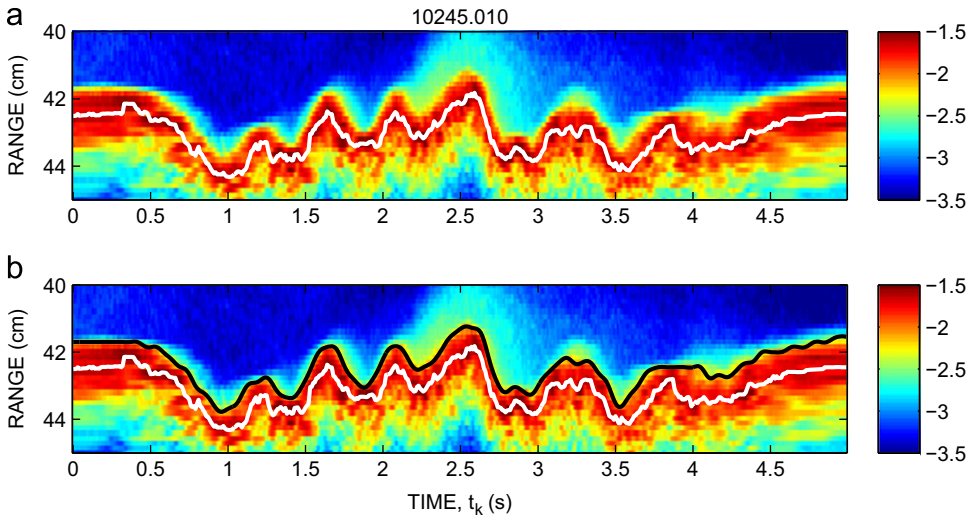

Fig. 4. Half-cycle segment of phase-averaged backscatter amplitude and the two estimates of range to the bed: $\overline{r}_b(t_k)$ (white) and $\overline{R}_B(t_k)$ (black). The colour scale indicates the backscatter amplitude in dB re 1 V. The white line and colour scale are identical in both panels. Comparing (a) and (b) indicates where the black line falls relative to the backscatter gradient. Elapsed time, t, after run initiation=34.7 min. The cycle-averaged values of $\overline{r}_b$ and $\overline{R}_B$ are 43.1 and 42.4 cm, respectively. (For interpretation of the references to colour in this figure legend, the reader is referred to the web version of this article.)

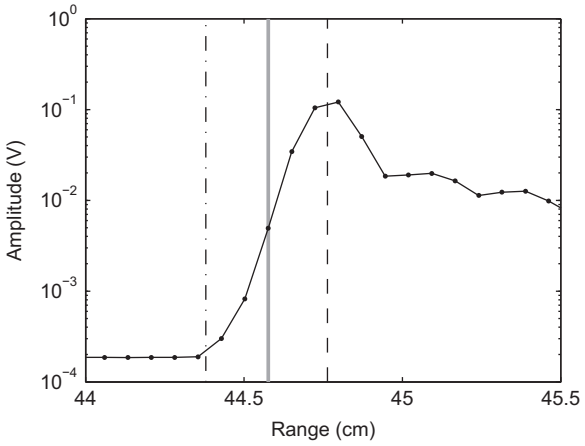

Fig. 5. Average 1.7 MHz backscatter profile from a stationary flat bed of the same sand as that used in the mobile bed experiments, showing the values r_b (dashed line) and R_B (grey line) computed for this ensemble-mean profile. The dash–dot line is the measured distance from the centre transducer to the sediment surface. r_b=44.8 cm; R_B=44.6 cm. 7-tap PFIR.

bed is

$$z_{Rmin} = \frac{1}{T_K}\int_0^{T_K} \overline{R}_B(t_k)\,\mathrm{d}t_k - \overline{R}_{Bmin} \tag{13}$$

where $\overline{R}_{Bmin}$ is the minimum value of $\overline{R}_B(t_k)$.

It is important to point out that the ca. 0.5 cm thick zone between $\overline{r}_b(t_k)$ and $\overline{R}_B(t_k)$ in Fig. 4 (i.e. between the white and black lines) cannot be attributed to a moving layer of sediment. That this cannot be the case is clear from the fact that, at t_k=0 and 5 s, the Kart velocity is zero, yet the zone $\overline{r}_b - \overline{R}_B$ is as thick or thicker at these times than when the Kart was moving at maximum velocity. The fact is that the envelope of the backscatter from a stationary rough bed normally rises gradually, not abruptly, from the background level to a maximum, as was demonstrated for fixed sand and gravel beds in Hay et al. (2012a). Fig. 5 shows that this is also true for a flat bed of the same sand as that used in the present experiments. The average of the backscatter amplitude profiles from the centre transducer at 24 horizontally separated positions over a carefully flattened and stationary 40 cm square and 8 cm deep bed of the blasting sand is shown. The horizontal separation between measurement points was 2.5 cm, i.e. greater than the 2 cm footprint of the sonar beam at 45 cm range (Hay et al., 2012a). The values of r_b and R_B are indicated: $r_b - R_B$ is several mm, comparable to the differences for the RippleKart run in Fig. 4. Also shown in Fig. 5 is the distance from the centre transducer to the sediment–water interface, measured with a possible error of $\pm$0.5 mm. This measurement corresponds exactly to the range at which the mean backscatter amplitude begins to rise above background, suggesting that if anything, R_B slightly overestimates the range to the sediment–water interface.

The velocity time series in each range bin were separated into low frequency and high frequency bands using a fifth-order Butterworth filter in both the forward and reverse directions with a 0.2 Hz cutoff frequency. This defined, for example, the horizontal velocity fluctuations, u', and the low-passed horizontal velocity, u_{Lo} (the latter by subtracting $u'(t)$ from the unfiltered u time series).

4. Results

4.1. Bed elevation profiles

The bed elevation profiles, $\eta(x)$, during the YD245 test are plotted in Fig. 6a. Each profile represents the first half-cycle of the difference between $\overline{r}_b(t_k)$ and its cycle mean, transformed to x using $x(t_k) = A\cos\omega t_k$ with $A = d/2$. The corresponding RMS elevations, σ_η, computed after linearly interpolating $\eta(x)$ at 2 mm intervals in x, are shown in Fig. 6b together with the results for the YD242 and YD246 tests. The time evolution of the bed elevation spectrum, $S_{\eta\eta}$ (also computed from $\eta(x)$ after interpolation to constant Δx), is shown in Fig. 6c for the YD245 test. These spectra exhibit the increase in variance with time indicated by the σ_η values, and also a continual increase in spectral energy density at low spatial frequencies, including a shift of the spectral peak towards lower frequencies for $t \lesssim 30$ min, consistent with the findings of Davis et al. (2004). At high spatial frequencies, the spectra exhibit a saturation range (i.e. the spectral densities remain approximately constant). A saturation range is also observed in the spectra of wind-driven surface gravity waves (e.g. Phillips, 1966). As for surface waves, it is likely that the

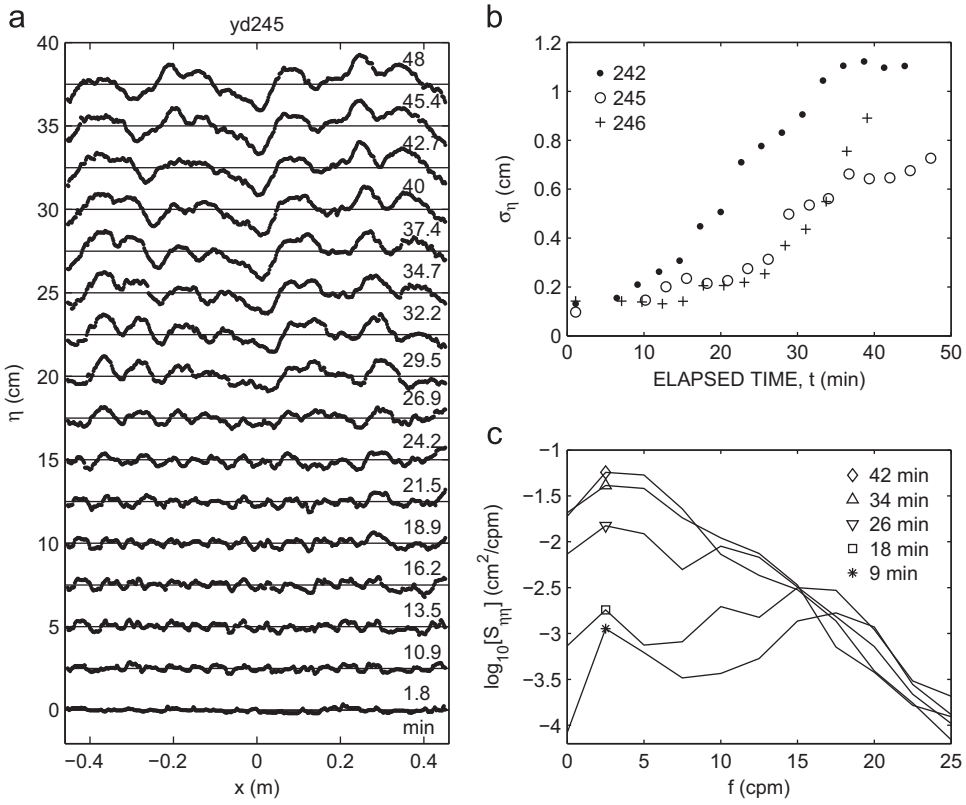

Fig. 6. (a) Bed elevation profiles during the test on YD245, 2010. Time increases from bottom to top, as indicated by the values of elapsed time (in minutes) on the right. Successive profiles are offset vertically by 2.5 cm. (b) Time evolution of RMS bed elevation, σ_η, during the tests on YD242, YD245 and YD246, 2010. (c) Bed elevation spectra, $S_{\eta\eta}$, for the YD245 trial. Each spectrum is the average of the spectra from four consecutive profiles in (a). The corresponding average times are indicated in the legend. $d=90$ cm.

existence of a saturation range in the spectra of growing ripple fields reflects a control on maximum steepness. For sand ripples developing under low energy forcing, as is the case here, the maximum angle of repose represents one control on steepness, and is indicated by the measured and modelled $S_{\eta\eta}$ spectra for rippled beds reported in Hay (2011). Under high energy forcing, below the transition to flat bed, high stresses at the bed are likely the dominant factor controlling steepness (e.g. Nielsen, 1981).

As elapsed time increased beyond 10 min, the RMS bed elevation varied substantially among the tests, by a factor of 2–4 (Fig. 6b). There are two main reasons for this difference. The first is that the ripples, which tended to be two-dimensional (i.e. long-crested) during the early stages of development, became highly three-dimensional as time progressed. This behaviour is demonstrated by the results in Fig. 7, which are the values of σ_η from bed profiles at three locations separated by 5 cm in the cross-tank direction: the σ_η values at the three locations are effectively the same until ca. 12–15 min elapsed time, at which point they diverge, corresponding to the transition from 2d to 3d ripples. These profiles were obtained with a laser light-sheet and calibrated camera, using methodology very similar to that described in Crawford and Hay (1998), except that instead of video the images were stills taken with a Nikon D80 digital camera (with the Kart stationary). The laser-camera approach could not be used for the MFDop runs because the seeding material resulted in the water being too cloudy, and thus the MFDop-measured bed profiles are used instead. Overall, the time courses of σ_η obtained from the MFDop data and those from the laser-Nikon data are similar; in particular, both data sets indicate a ca. 0.6–0.8 cm maximum value for σ_η after ca. 30 min run time, both exhibit differences developing at 10–15 min run time, and both exhibit plateaus separated by S-shaped transitions similar to

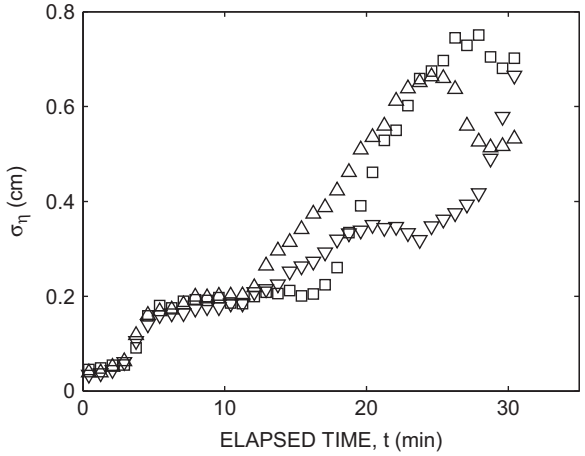

Fig. 7. RMS bed elevation, σ_η, determined photogrammetrically using a laser light sheet. The three sets of points are from profiles indicated by the different symbols obtained at the same times but at three y-positions, one at the tank centreline, the other two offset from the centreline by ± 5 cm. As explained in the text, these data are from a test on YD056, 2009, i.e. they are not contemporaneous with the data in Fig. 6. $d=90$ cm.

those observed by Davis et al. (2004) and Testik et al. (2005). The initial values of σ_η are lower in the laser-camera data compared to the MFDop results. This difference is to be expected both because the laser-camera elevation data are less noisy (since the bed was stationary with no sand in suspension) and because, in the case of the MFDop profiles, the high turbidity associated with the fine-grained seeding material made it more difficult to verify that the bed was flat prior to initiating each experiment.

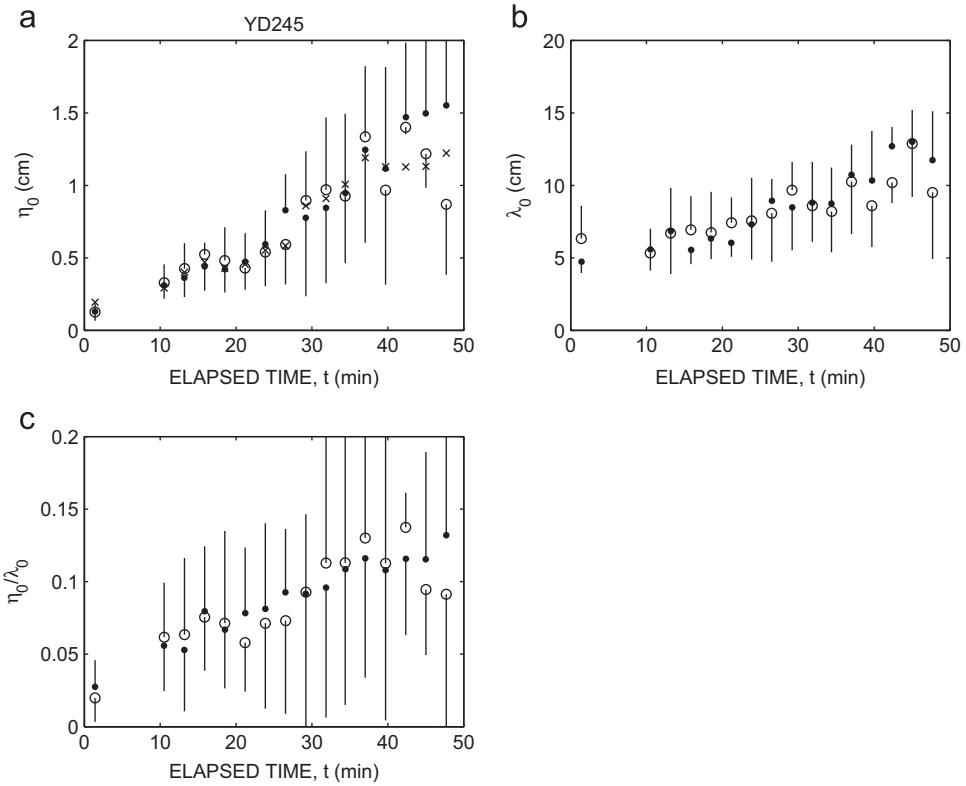

Fig. 8. Time evolution of ripple properties from a zero-crossing analysis of the profiles in Fig. 6a: (a) height, η_0; (b) wavelength, λ_0; and (c) steepness, η_0/λ_0. Open circles are from the down-crossings; solid circles from the up-crossings. Error bars represent + or − one standard deviation (only half error bars are shown to avoid overlap). The × symbols in (a) indicate $2\sigma_\eta$. YD245.

4.2. Ripple wavelength, height and steepness

Fig. 8 shows the time evolution of ripple height, η_0, wavelength, λ_0, and steepness, η_0/λ_0. The heights and wavelengths were determined from a zero-crossing analysis of the elevation profiles in Fig. 6a, after low-pass filtering to remove high-frequency noise at spatial frequencies above 30 cpm. The zero-crossings were obtained from the phase of the Hilbert transform of the first derivative of the low-passed elevation profile. Heights and wavelengths were estimated from both the up-crossings and down-crossings: that is, for the up-crossings, η_0 is the vertical distance between the trough and following crest, while λ_0 is twice the horizontal distance between these points, and similarly for the down-crossings. Both up- and down-crossings were used because, for irregular bed profiles like those in Fig. 6a, the two estimates for a single ripple can be quite different. As indicated in Fig. 8a and b, both height and wavelength increase with time on average (consistent with Fig. 6). The steepnesses also increased with time, from about 0.03 to 0.10 on average. The wide error bars in Fig. 8, which represent + or − one standard deviation from the mean, reflect the broad spectral content of the evolving bed profile.

The average ripple wavelength did not exceed 15 cm (Fig. 8b), and the maximum wavelength did not exceed 30 cm (Fig. 6a). Both values are significantly less than the wavelength of orbital-scale ripples (i.e. 0.6d to 0.7d: Clifton and Dingler, 1984; Wiberg and Harris, 1994; Traykovski et al., 1999) i.e. 54–63 cm here, indicating that the ripples were far from reaching the final equilibrium state even at 50 min elapsed time. Given the 2 m length of the tray and the 10 cm depth of the sand, end effects and scour down to the base of the sand would have a pronounced influence on ripples of this size. Further, our experience with the Kart apparatus to date indicates that, for $d > 80$ cm, once the ripples become three-dimensional, transition back to a two-dimensional state has never occurred. Consequently, we did not attempt to reach the equilibrium orbital ripple state in these experiments.

The additional points in the ripple height panel (Fig. 8a), indicated by the symbol ×, represent

$$\eta_0 = 2\sigma_\eta \tag{14}$$

which is half of what would be the "significant" ripple height if the heights were Rayleigh-distributed (i.e. the equivalent of the significant height of surface gravity waves: see Thornton and Guza, 1983). As these points fall well within the bounds determined by the mean heights determined from the zero-crossing analysis, Eq. (14) is used as the measure of ripple height later in the paper, Section 4.8.

4.3. Phase-averaged horizontal velocities

The phase-averaged horizontal velocity in the lab frame is shown in Fig. 9a. The motion of the Kart during the two half-cycles is clearly indicated for range bins within the bed (i.e. $r \gtrsim 42$ cm). The interface between the bed and the overlying water undulates with time as ripples pass beneath the MFDop location. At shorter ranges, diffusion of horizontal momentum upward away from the bed is evident, lagging increasingly far behind the Kart motion with increasing height. Fig. 9b shows the same data in the frame of reference moving with the Kart: the phase lead characteristic of oscillatory boundary layer flow is apparent. Panel (c) shows the phase-averaged correlation magnitude. In (pulse-to-pulse) coherent Doppler, velocity is estimated from the rate of change in phase of sound scattered from a fixed range. The fundamental measurement is the ensemble-averaged complex correlation between N consecutive pulses,

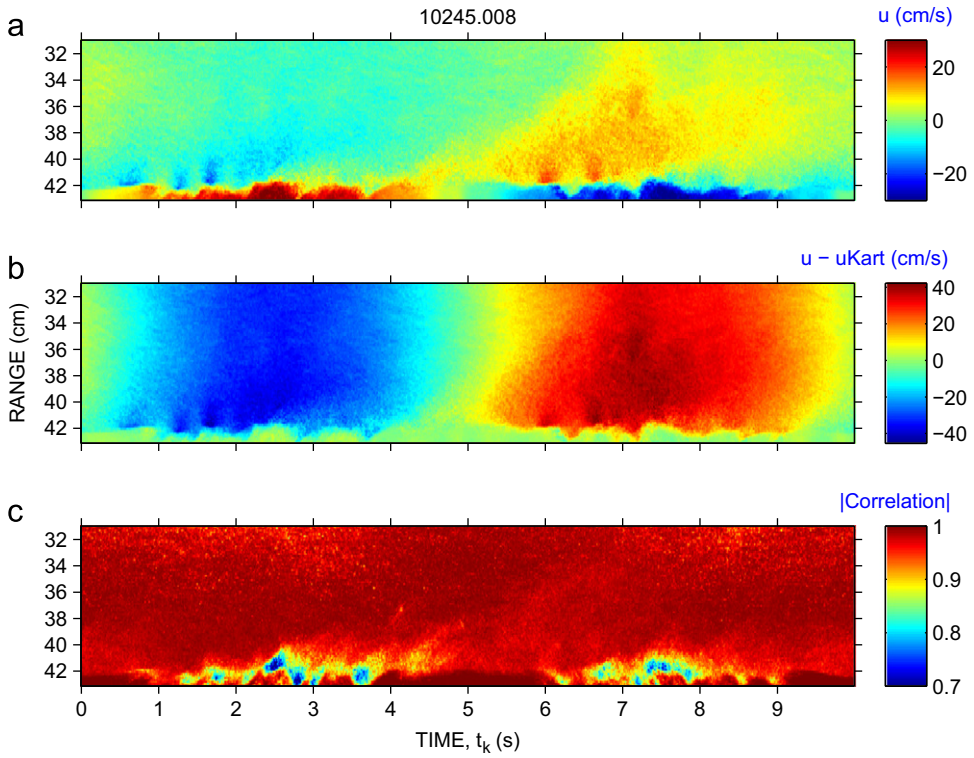

Fig. 9. (a) Phase-averaged horizontal velocity in: (a) the lab frame and (b) the frame of reference moving with the Kart, i.e. $\hat{u}$ given by Eq. (2), with $\hat{u}_\infty = -u_K$. (c) Phase-averaged correlation magnitude. Elapsed time $t=30.6$ min. (For interpretation of the references to colour in this figure legend, the reader is referred to the web version of this article.)

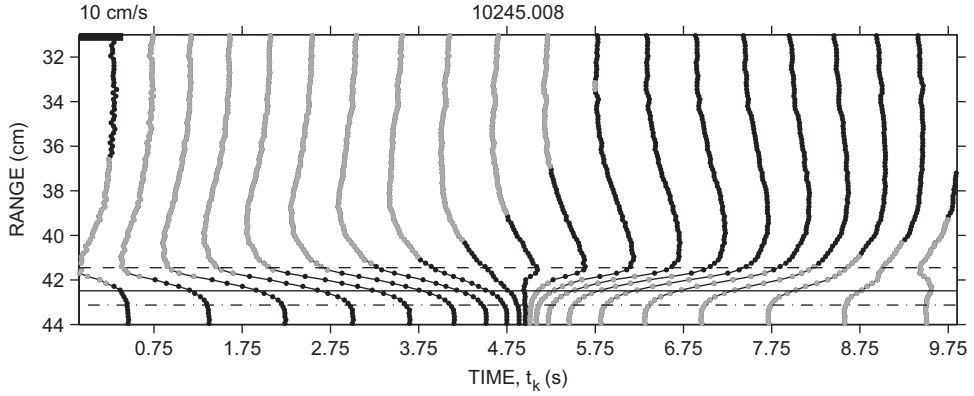

Fig. 10. Vertical profiles at 0.5 s intervals of phase-averaged horizontal velocity, u_{Lo}, in the lab frame. Black dots indicate positive values; grey negative. The horizontal dashed and solid lines indicate $\overline{R}_{Bmin}$ and the cycle-average of $\overline{R}_B(t_k)$ respectively; the dash–dot line indicates the cycle-average of $\overline{r}_b$. Successive profiles are offset by 10 cm/s. Elapsed time $t=30.6$ min.

$\langle \varrho \rangle$ (see Zrnic, 1977, for example). As implemented in the MFDop, $\langle \varrho \rangle$ takes the form

$$\langle \varrho \rangle = \sum_{j=1}^{N-1} z_j^* z_{j+1} \Big/ \sum_{j=1}^{N-1} |z_j^* z_{j+1}| \tag{15}$$

where $z_j = a_j \exp(i\phi_j)$ is the complex amplitude of the return from the jth pulse, and $*$ represents the complex conjugate. The correlations in panel (c) represent the magnitude of $\langle \varrho \rangle$. Low values develop in a thin region close to the bed in the neighbourhood of maximum Kart speed (i.e. near $t_k=2.5$ and 7.5 s). As discussed by Hay et al. (2012a) in relation to comparable data above a bed of fixed gravel, these low correlation zones near the bed are associated with turbulence.

Vertical profiles of phase-averaged u_{Lo} through the course of the oscillation cycle are plotted at 0.5 s intervals in Fig. 10. Note that these profiles are in the lab frame (i.e. u, not $\hat{u}$), and thus can be compared to the unfiltered u data in Fig. 9a. The occurrence of flow reversal in the boundary layer first, before reversal in the interior, is clearly evident (e.g. at $t_k \sim 5$ s and $t_k \sim 10$ s). Also shown, as dashed, solid, and dash–dot lines, are the minimum and cycle-averaged values of $\overline{R}_B$, and the cycle-averaged value of $\overline{r}_b$ (see Eqs. (9), (12), and (13) and related text). Note that $\overline{u}_{Lo}$ becomes relatively independent of range, and therefore representative of the Kart velocities, only for ranges at and beyond the cycle-averaged value of $\overline{r}_b$, indicating why the MFDop estimates of Kart velocity were made at $\overline{r}_b(t_k)$.

Example $\hat{u}_0(z)$ and $\hat{\phi}_0(z)$ profiles (see Eq. (3)) at three different times during the YD246 test are shown in Fig. 11, illustrating the growth of the boundary layer as ripple heights increased through time. The solid grey points indicate the height, z_{Rmin}, corresponding to the minimum range to the bed (Eq. (13)). In the fixed

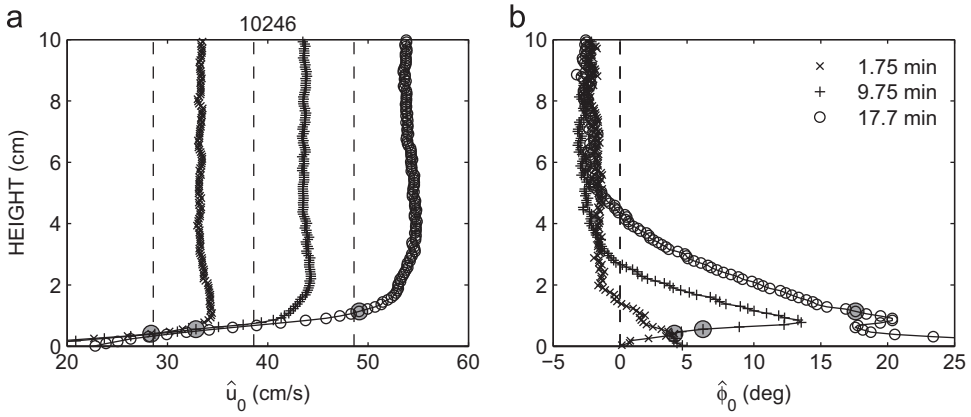

Fig. 11. Vertical profiles of (a) $\hat{u}_0$ and (b) $\hat{\phi}_0$, the magnitude and phase of the horizontal velocity in the frame of reference moving with the Kart, during ripple development at the three values of elapsed time indicated in the legend. The successive $\hat{u}_0$ profiles in (a) are offset by 10 cm/s. The solid grey circles indicate the heights corresponding to $\overline{R}_{Bmin}$, the minimum range to the bed (see Eq. (13)). Single-frequency run on YD246 (see Table 2).

roughness experiments, the profiles of $\hat{\phi}_0(z)$ increased monotonically towards the bed, reaching a peak at or immediately above z_{Rmin} (Hay et al., 2012a). The $\hat{\phi}_0(z)$ profiles in Fig. 11b exhibit similar monotonic increases as the bed is approached, but only up to a point. Early in the run, when ripple amplitudes were very small, the value of $\hat{\phi}_0(z)$ at z_{Rmin} is similar to the ca. 5° value at the mean bed level, $z=0$, and much less than the 20–30° maximum phase lead expected for turbulent oscillatory flow boundary layers. Higher values of $\hat{\phi}_0(z)$ are not observed for the low amplitude ripples because the boundary layer is so thin that the portion of the boundary layer immediately adjacent to the bed in which the larger phase leads occur is not resolved by the MFDop. A similar effect was observed in the fixed sand roughness measurements reported in Hay et al. (2012a). Ten minutes into the run, when the ripple amplitudes had increased to ca. 0.2 cm RMS (Fig. 6b) and the boundary layer was thicker, the $\hat{\phi}_0(z)$ profile exhibits a pronounced peak near the bed. A similar peak is also present in the later profile at 18 min when σ_η was ca. 0.2–0.5 cm, by which time the maximum value of $\hat{\phi}_0(z)$ approached 20°. For the profiles at 10 and 18 min, the value of z_{Rmin} is 3–4 range bins (i.e. ≤ 3 mm) above or below the peak.

The relative positions of z_{Rmin} and the peak in $\hat{\phi}_0(z)$ in Fig. 11b near $z=1$ cm at run times of 10 and 18 min bring up the question raised in Section 2 of the relative locations of the hydrodynamic and acoustic bed levels. A near-bed peak in $\hat{\phi}_0(z)$ is unexpected: the LDA measurements made by Jensen (1988), for example, exhibit a monotonic increase to a maximum value which then remains constant as the bed is approached (see also the comparisons in Hay et al., 2012a). In contrast, for range bins closer to the bed than the peak, $\hat{\phi}_0(z)$ is far from constant.

Because the amplitude of the bottom return is very large compared to that of the backscatter from the particles in suspension, the MFDop measurements of particle velocities immediately above the bed are contaminated. Some of this contamination is associated with the beam geometry, some due to the impulse response of the digital filters implemented in the receiver. For the fixed roughness experiments, the thickness of the near-bed contamination zone relative to $\overline{R}_B$ was determined to be 5 ± 1 mm, based both on the height at which the phase lead reached its first maximum, and on the height at which the velocity profile first departed from logarithmic. The height of the $\hat{\phi}_0$ peak is comparable, ca. 7 or 8 mm. This fact, together with the proximity of the peak to z_{Rmin}, indicate to us that the values of $\hat{\phi}_0$ below the z-level of the peak cannot be trusted and, by implication, neither can the corresponding values of $\hat{u}_0$.

The $\hat{u}_0(z)$ profiles in Fig. 11a exhibit the expected overshoot, relative to the values far above the bed. However, these latter values exceed the value of U_{K0}, indicated by the vertical dashed lines, by ca. 5 cm/s or 20% of the 28.3 cm/s maximum Kart speed for $d=90$ cm. A similar, but smaller (ca. 4%), effect was observed for the fixed gravel bed experiments, and the effect was essentially nil for the fixed sand bed. This amplification of the apparent velocity relative to the Kart in the interior is due to the reaction flow induced in the tank in response to the displacement of ambient water by the sediment-laden tray. The vertical thickness of the tray and its fixed or mobile sediment load are: 0.64 cm for the fixed sand bed; 1.64 cm for the fixed gravel bed; and $\gtrsim 10$ cm for the mobile sand bed. Thus, the magnitude of the reaction flow increases in proportion to the vertical thickness of the tray.

The phases at large distances from the bed are roughly constant but non-zero, being ca. $-2°$ to $-3°$ (Fig. 11b). Similar values were observed in the fixed roughness data: ca. $-2°$ for the gravel, and ca. $-1°$ for the sand. A phase difference of 1–3° corresponds to between 2 and 7 samples at our 85 Hz sampling rate and 10 s oscillation period. While a consistent 1 or 2 sample offset due to timing errors might be possible, a consistent 5–7 sample difference among three separate experiments is unlikely. Since the magnitude of the phase offset increases with the magnitude of the reaction flow, it is suggested that the phase offset is also associated with the reaction flow.

4.4. Defect stress

The defect stress was computed from the profiles of $u_{Lo}(z,t)$ using Eq. (6). Fig. 12 shows an example set of results from one of the YD245 runs. As indicated in the top panel: (1) large magnitude defect stresses are generated at the bed close to the Kart speed maxima at 2.5 and 7.5 s which then diffuse upward, decaying with increasing height; (2) negative defect stresses are generated at the bed during the first half-cycle, positive stresses during the second; and (3) subsequently the stress diffuses upward away from the boundary, the magnitude decreasing with increasing height, leading to stress inversions as stress of one sign encounters stress of the opposite sign from the previous half-cycle.

The vertical structure of the acceleration defect integral at the times of maximum defect stress during each half-cycle is shown in Fig. 12b. The data points are plotted only for heights greater than z_{Rmin}. These profiles tend to be quite linear close to the bed. As in Hay et al. (2012b), this linearity is exploited to extrapolate

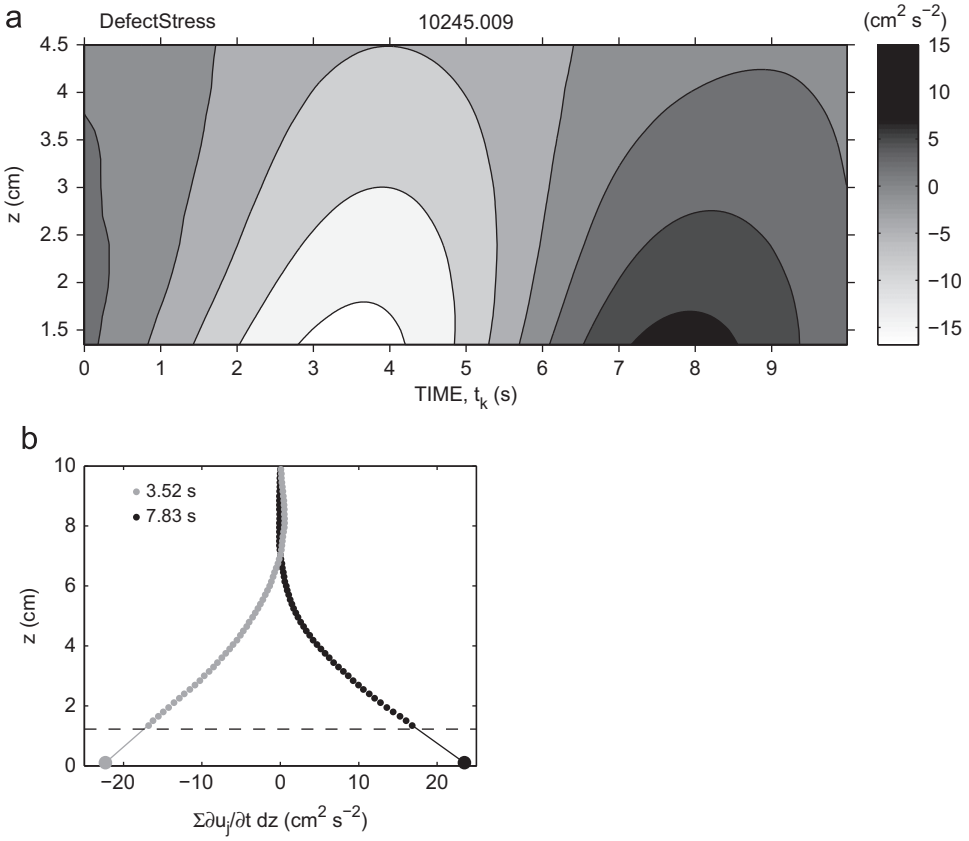

Fig. 12. Defect stress. (a) Contours of the defect stress during the oscillation cycle (10 cm^2/s^2 contour interval). (b) Profiles of the vertically integrated defect stress at the indicated times during each half-cycle when the integral was a maximum. Larger solid circles represent the linear extrapolation to z_0=1 mm (see Fig. 14c and related discussion in the text). Dashed lines indicate z_{Rmin}. Elapsed time t=32.2 min.

the profile to the bed to obtain the bottom stress estimates indicated by the large solid circles. The lower limit of integration was set at z=1 mm. This choice was based on the values of z_0 obtained via the law-of-the-wall, presented in Section 4.6.

4.5. Reynolds stress

The Reynolds stresses were estimated from the difference between the second moment of the velocities projected onto the bistatic geometry of the sonar. The advantage of this approach over the usual "direct" eddy correlation estimate (i.e. that obtained from the product of u' and w') is that spurious correlations due to the horizontal separation of the measurement volumes for the two bistatic beam pairs (see Fig. 3) do not contribute to the estimate (Hay et al., 2012b). Instead, it is only required that the second moments of the turbulent velocity fluctuations be homogeneous on the scale of the horizontal separation between the measurement volumes. For the MFDop, these separations are less than 5 cm. Note that Hurther and Lemmin (2001) also compute the Reynolds stress in this manner. However, their use of a shaped transmit transducer to generate a collimated centre beam largely eliminates the horizontal separation between measurement volumes, but also precludes the use of multiple frequencies.

Fig. 13a and b shows the phase-averaged Reynolds stress for one of the later YD245 runs when the ripples were well-developed, as a function of range and time during each half-cycle, with the sediment–water interface profile, $\overline{R}_B(t_k)$, superimposed. Like the defect stress, the Reynolds stress is dominantly negative during the first half-cycle, and dominantly positive during the second. In addition, the temporal pattern exhibited by the zones of high Reynolds stress during each half-cycle is clearly modulated by the passing spatial structure of the ripples. Fig. 13c shows the vertical structure of the Reynolds stress at the times corresponding the overall peak stress in each half-cycle. The locations of these peaks, relative to the cycle time and the bed profile, are also indicated by the open circles in panels (a) and (b). These peak stresses were determined as follows. First, the phase-averaged stress was block-averaged in non-overlapping 0.1 s time intervals, so as to reduce noise. Second, the peak stress in each 0.1 s interval was found. Third, the overall peak stress in each half-cycle was defined to be the maximum of these values, subject to the condition that its vertical location be more than 5 mm above the local bed level (to be assured that the estimates were not contaminated by the bottom return).

4.6. Stress from the law of the wall

Profiles of phase-averaged $u_{Lo}(z,t_k)$ for the same YD245 run as Fig. 13 are plotted in Fig. 14a at 0.5 s intervals during the first half-cycle, together with the best fits of $\overline{u}_{Lo}(z,t_k)-u_K(t_k)$ to $a[\ln z+b]$. The profiles, which begin at z_{Rmin} (Eq. (13)) plus 0.5 cm, exhibit the characteristic $\log z$ behaviour near the bed, the vertical extent of which grows during the half-cycle until, during the deceleration phase (i.e. after t_k=2.5 s), the logarithmic zone spans essentially the entire profile. The $\overline{u}_{Lo}$ profiles and fitted parameter values are not shown for times close to 0 and 5 s, when u_K is zero: the fits close to these times yielded complex rather than real values for u_* and Δz, because of flow reversal in the boundary layer. Jensen et al. (1989) also observed that the fitting procedure fails near the u_K zero-crossings.

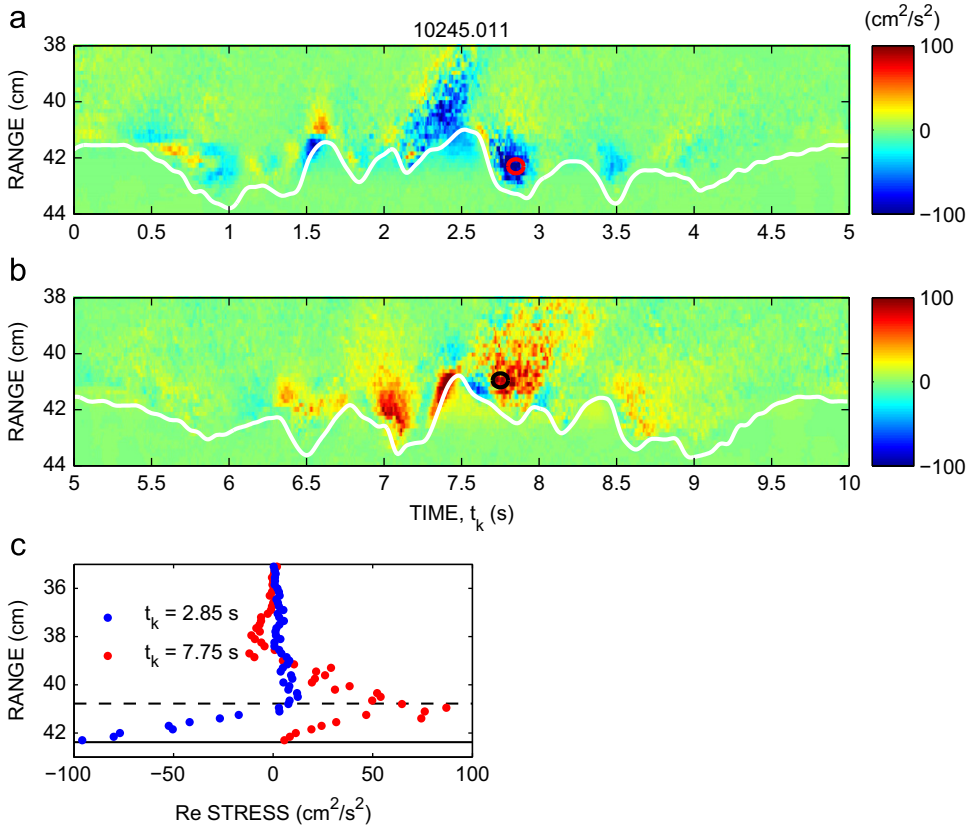

Fig. 13. Phase-averaged Reynolds stress during (a) the first half-cycle, and (b) the second half-cycle. The undulating white lines in (a) and (b) denote the bed level, $\overline{R}_B(t_k)$. The red circle in (a) and black circle in (b) indicate the half-cycle Reynolds stress extrema, as defined in Section 4.5. Panel (c) shows the 0.1 s averaged profiles at the times of these extrema. The dashed and solid lines in (c) indicate min $\overline{R}_B(t_k)$ and the cycle average of $\overline{R}_B(t_k)$. Elapsed time $t=37.4$ min. (For interpretation of the references to colour in this figure legend, the reader is referred to the web version of this article.)

The best-fit values of u_* and z_0 are plotted in panels (b) and (c) of Fig. 14, together with their 95% confidence intervals. These intervals are small for u_*, but considerably wider for z_0. The value of z_0 near the peak stress is ca. 1 mm for this run. The u_* variations in Fig. 14b are quasi-sinusoidal and lag the Kart velocity (the vertical dashed lines in Fig. 14b indicate the mid-point of each 1/2 cycle, i.e. the maximum Kart speed). The sign of these stress estimates is consistent with the signs of the defect stress and Reynolds stress in Figs. 12 and 13 on half-cycle time scales, i.e. all three estimates of the near-bed stress are dominantly negative during the first half-cycle, and dominantly positive during the second.

4.7. u_{*m} vs. σ_η

The values of u_{*m} obtained from the defect stress and Reynolds stress methods for all of the data runs in all three trials are plotted vs. σ_η in Fig. 15. Both sets of results exhibit trends towards higher values of u_{*m} with increasing σ_η, and comparable degrees of scatter both among the points for a given trial and between trials. However, the trend with σ_η is steeper for the Reynolds stress data, such that the u_{*m} estimates at higher values of σ_η are a factor of 2 *larger* than the defect stress estimates. This result is very different from our results for fixed gravel beds (Hay et al., 2012b). In those experiments, the u_{*m} values from the maximum Reynolds stress were a factor of 2 *lower* than the estimates based on the defect stress.

The law-of-the-wall estimates of u_{*m} are plotted in Fig. 16. For $\sigma_\eta \lesssim 0.2$ cm, the YD242 estimates are anomalously high, while the YD245 and YD246 results are lower than the ca. 2 cm/s values indicated by the other two methods. For $\sigma_\eta \gtrsim 0.2$ cm, the log law estimates are essentially constant at ca. 4 cm/s such that, for $\sigma_\eta \sim 1$ cm, they are 20–30% *lower* than the defect stress values. In the fixed gravel experiments, the law-of-the-wall estimates of maximum stress differed from the defect stress estimates by 50% (Hay et al., 2012b), corresponding to 25% *higher* values of u_{*m}.

4.8. The bed friction factor, f_w

Observed values for the friction factor were determined from Eq. (8) with

$$U_{0\infty} = U_{K0} + u_{0\infty} \tag{16}$$

where $u_{0\infty}$ is the observed amplitude of u in the lab frame farthest from the bed. Thus, $U_{0\infty}$ is the amplitude of the Kart speed plus the amplitude of the reaction flow.

For fixed roughness beds, Swart (1974) proposed the empirical relation

$$f_w = \exp[5.213(r_h/A)^{0.194} - 5.977] \tag{17}$$

where r_h is the hydraulic roughness of the bed, and A is the semi-excursion of the interior flow immediately outside the boundary layer. Based on results from later laboratory experiments, including those reported by Sleath (1987) and Jensen et al. (1989), Nielsen (1992) suggested that the numerical coefficients in Eq. (17) should be modified, i.e.

$$f_w = \exp[5.5(r_h/A)^{0.2} - 6.3] \tag{18}$$

We note in passing that estimates of f_w obtained via the defect stress method from the fixed gravel bed experiments with the MFDop are in good agreement with Eq. (18) (Hay et al., 2012b).

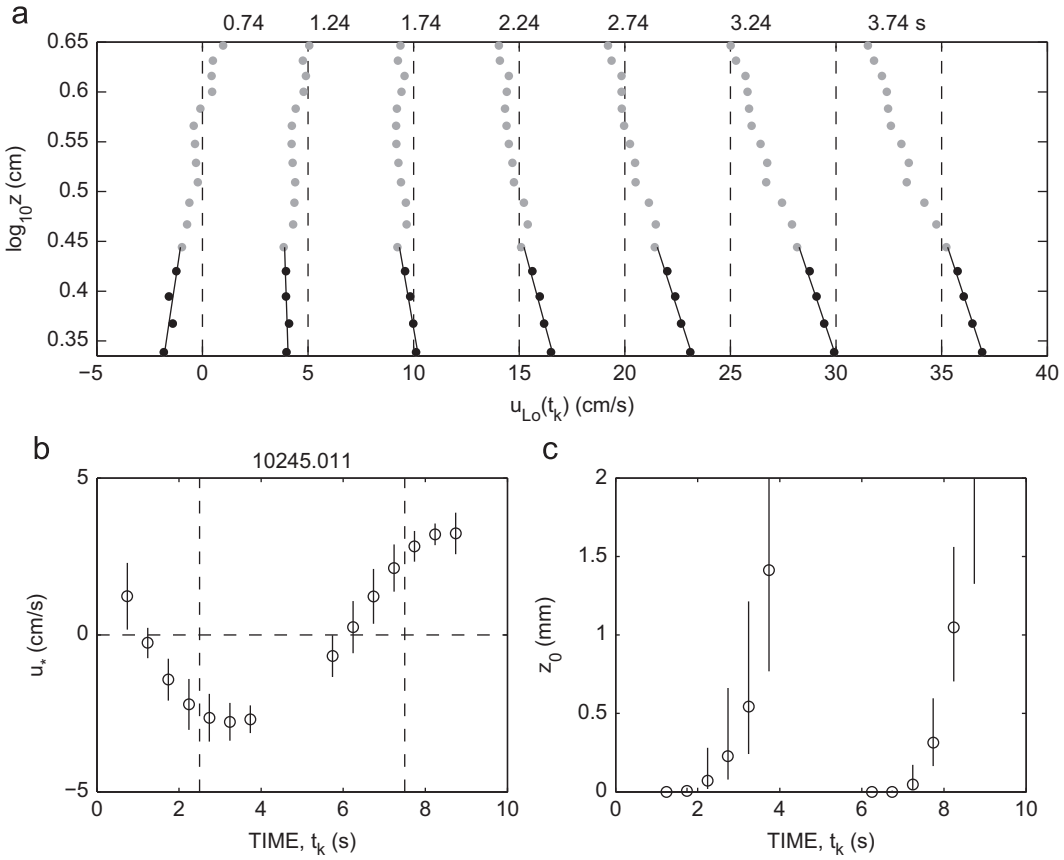

Fig. 14. Law-of-the-wall results. (a) Profiles of $u_{Lo}(z,t_k)$ plotted vs. z at 0.5 s intervals during the first half-cycle (solid circles). Successive profiles are offset by 5 cm/s. Vertical dashed lines indicate $u=0$. Profile times (t_k) are along the top border of the panel. Solid lines are the best-fits to the points in black. Panels (b) and (c) show the best-fit values of u_* and z_0 vs. time. The dashed vertical lines in (b) indicate the mid-point of each half-cycle. Solid vertical lines in (b) and (c) are 95% confidence intervals. Elapsed time $t=37.4$ min.

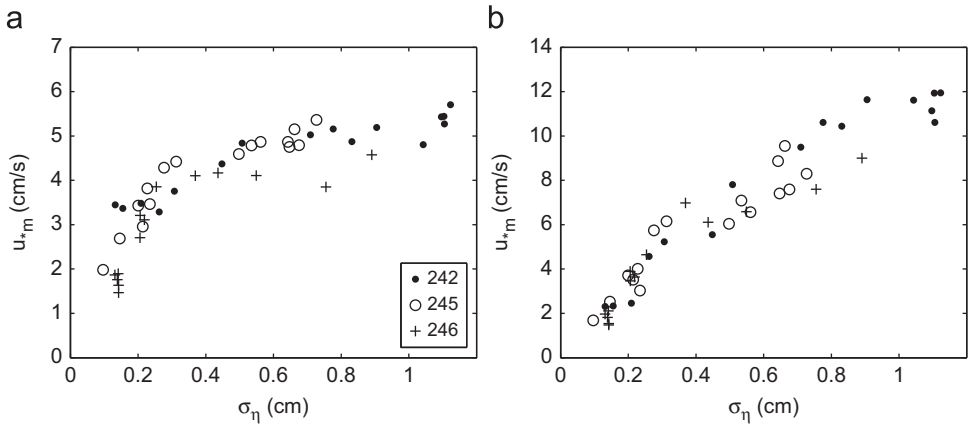

Fig. 15. u_{*m} vs. σ_η from: (a) the defect stress, DS; and (b) the Reynolds stress, RS. Each data point is the average of two u_{*m} estimates, one from each half-cycle. Note the factor of 2 difference in the y-axis scales in the two panels.

For fixed roughness beds, the hydraulic roughness is the equivalent Nikuradse sand roughness, k_N, usually taken to be a multiple of the median grain size. Sleath (1987) used $2D_{50}$; Jensen et al. (1989) $2.5D_{50}$. The question of interest for rippled beds is what is the relationship between hydraulic roughness and the geometric roughness of the ripples. Nielsen (1992) examined this question in the light of the then available data, finding for low to moderate energy forcing conditions that

$$r_h = \Lambda\eta_0 \tag{19}$$

where $1<\Lambda<3$. The forcing energy was characterized by the grain roughness Shields parameter, $\theta_{2.5}$, low to moderate energy corresponding to $\theta_{2.5}\lesssim 0.5$. The Shields parameter is given by

$$\theta_{2.5} = \frac{f_{2.5}U_0^2/2}{(s-1)gD_{50}} \tag{20}$$

where s is the specific gravity of the sediment grains and, following Nielsen (1992, p. 105), $f_{2.5}$ is computed using Eq. (17) with $r_h = k_N = 2.5D_{50}$. Here, $\theta_{2.5}=0.11$. Predictions based on Eqs. (18) and (19) are compared to the observed values in

Fig. 17a, the latter computed from the defect stress estimates of u_{*m} using Eqs. (8) and (16). The comparison indicates overall consistency with predicted dependence on ripple height for Λ between 1 and 3, in agreement with the range of values compiled by Nielsen (1992). (Note to the reader: here and throughout the remainder of this article, k_N and r_h are used to distinguish the hydraulic roughness of fixed-roughness and mobile beds, respectively.)

The geometric roughness of any rough boundary is also partly characterized by the spacing of the roughness elements which, in the case of a rippled bed corresponds to the ripple wavelength. Nielsen investigated the effect of ripple wavelength by including a dependence on steepness, and proposed a second relation for r_h

$$r_h \sim 8\eta_0^2/\lambda_0 + 170 D_{50}\sqrt{\theta_{2.5}-\theta_c} \tag{21}$$

where $\theta_c \sim 0.05$ is the critical Shields parameter corresponding to the threshold of grain movement. Consider only the first term on the r.h.s. for the moment, rewritten as

$$r_h = 8\Gamma\eta_0^2/\lambda_0 \tag{22}$$

where the parameter Γ can be adjusted to fit the data. For the data summarized by Nielsen (1992, Fig. 3.6.8), $0.5 \lesssim \Gamma \lesssim 4$. The (defect stress) observed values of f_w are compared to predictions based on Eqs. (18) and (22) in Fig. 17b: $\Gamma \sim 3$ is indicated. Comparing Fig. 17a and b, including the ripple steepness factor appears to lead to improved agreement with the predicted form of f_w, especially for lower values of the roughness.

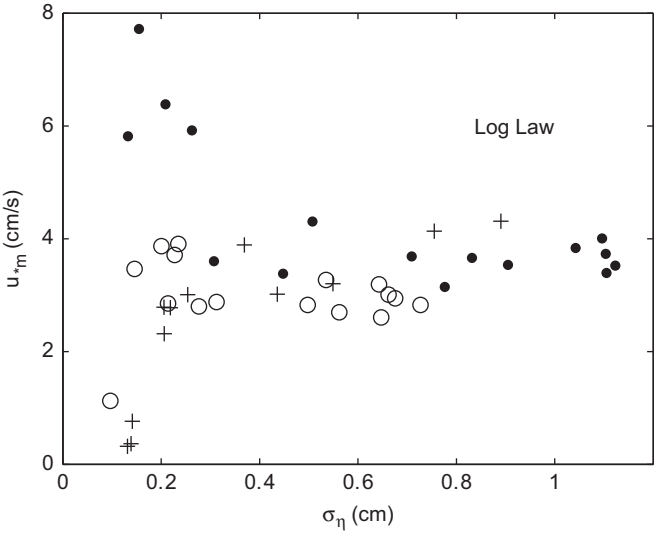

Fig. 16. u_{*m} from the law-of-the-wall vs. σ_η. Symbols as in Fig. 15.

Before proceeding, several points of clarification concerning the predicted values of f_w are needed. First, the ripple height η_0 was set to $2\sigma_\eta$, as per Eq. (14) and Fig. 8a. Second, based on Fig. 8c, the ripple steepness was computed using

$$\eta_0/\lambda_0 = 0.040 + 0.0022t \tag{23}$$

where t is the elapsed time in minutes, based on Fig. 8c. Third, the predicted values of f_w were obtained using Eq. (18), whereas Nielsen based his estimates on Eq. (17). The former relation is used here to be consistent with the facts that (a) Nielsen's modified form of Swart's relation is based on a more extensive data set, and (b) the overall better agreement with the measurements for fixed roughness in the sand and gravel size range (Hay et al., 2012b). The use of Eq. (18) leads to larger values for the hydraulic roughness, i.e. for the same value of the f_w, Eqs. (17) and (18) lead to

$$\frac{r_{h2}}{A} = \left[0.95\left(\frac{r_{h1}}{A}\right)^{0.194} + 0.059\right]^5 \tag{24}$$

where r_{h2} and r_{h1} are the roughness estimates using the Nielsen and Swart relations respectively. For $0.1 \le r_{h1} \le 2$ cm, which spans the range of the hydraulic roughnesses in Fig. 17, and $A \sim 50$ cm, it follows that r_{h2} is 100% to 50% larger than r_{h1}, indicating why the values of f_w in Fig. 17a tend to fall closer to the $\Lambda = 3$ curve. It does not, however, by itself explain the fact that $\Gamma \sim 3$, i.e. greater than the factor of 1.5–2 indicated by r_{h2}/r_{h1}. It is suggested that the additional factor of 2 is related to the low steepness ($\lesssim 0.1$) of the (evolving) ripples reported here compared to the steepnesses of equilibrium orbital-scale ripples under regular waves (0.2, see Nielsen, 1981, 1992).

Continuing, also plotted in Fig. 17b is the prediction based on Eq. (21), which can be compared to the curve for Eq. (22) with $\Gamma = 1$. It is clear that including the additional term on the r.h.s. of Eq. (21) leads to poorer agreement with the data, the reason being that the value of this term (0.9 cm) is larger than or comparable to the observed values of $8\eta_0^2/\lambda_0$. The data in Fig. 17 at low roughness values tend towards the predicted fixed grain roughness value, indicating that moving grains did not contribute measurably to the observed hydraulic roughness during the early stages of ripple development.

Thorne et al. (2002) have also found that $\Gamma \sim 3$: that is, their parameter δ equals $\Gamma/8$, and δ was estimated to be 24 ± 0.5. Importantly, the result obtained by Thorne et al. (2002) was based on measurements of the suspended sediment profile above equilibrium sand ripples in a large-scale wave flume, whereas

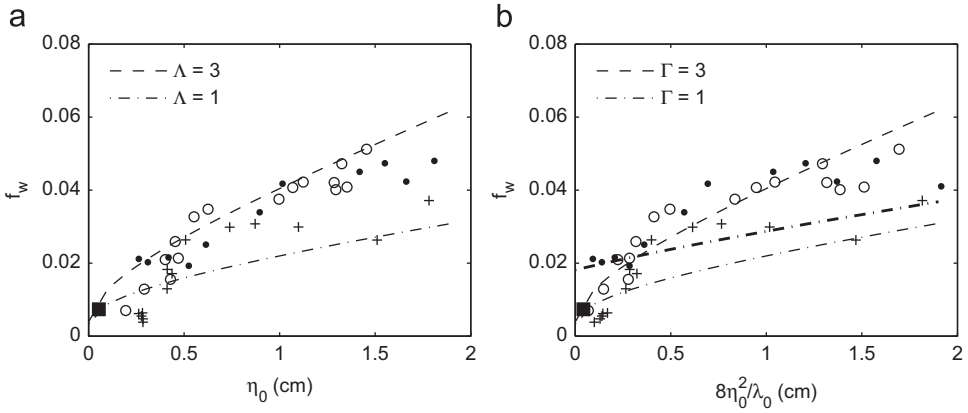

Fig. 17. f_w from the defect stress vs. ripple roughness. The ripple height $\eta_0 = 2\sigma_\eta$. (a) f_w vs. η_0. The dashed and dash–dot lines are Eq. (18) with $r = \Lambda\eta_0$. (b) f_w vs. $8\eta_0^2/\lambda_0$, showing the effect of ripple steepness. The thin dashed and dash–dot lines are Eq. (18) with $r_h = 8\Gamma\eta_0^2/\lambda_0$. The solid dash–dot line is Eq. (18) with r_h given by Eq. (21). The solid black square indicates f_w with $r_h = k_N = 2.5D_{50}$, plotted at $2.5D_{50}$ on the x-axis. Other symbols indicate YD242, 245, and 246 results (see Figs. 15 and 6b).

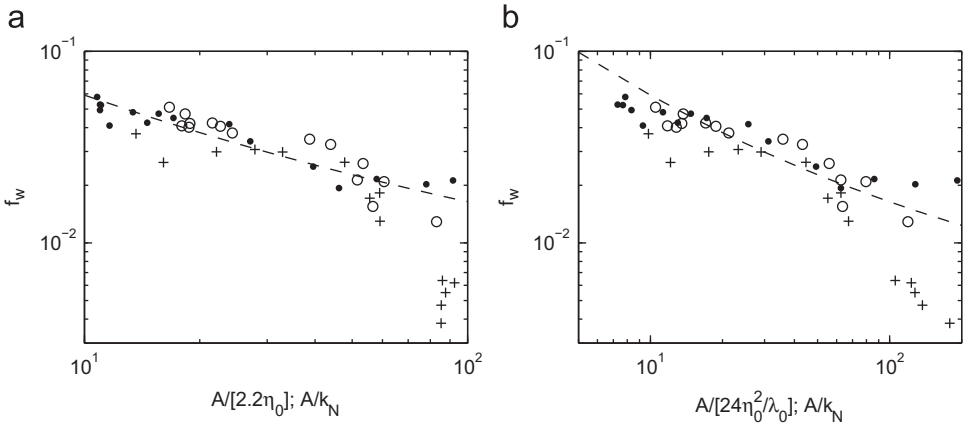

Fig. 18. f_w from the defect stress vs. reciprocal relative roughness. The dashed line is Nielsen's modification of Swart's relation for f_w vs. A/k_N. In (a), the points are the defect stress estimates of f_w vs. $A/[2.2\eta_0]$; in (b) f_w vs. $A/[24\eta_0^2/\lambda_0]$, i.e. with the steepness included. In both panels, the ripple height $\eta_0 = 2\sigma_\eta$. Symbols as in Fig. 15.

the present result is based on the velocity profile above evolving sand ripples on an oscillating bed. That two different types of measurement should lead to the same result supports a value close to 3 for Γ in Eq. (22).

4.9. f_w and relative roughness

The friction factor is plotted vs. the reciprocal relative roughness parameter, A/r_h, in Fig. 18 on a log-scale to facilitate comparison with previous work. The 10–200 range of A/k_N can be compared, for example, to the 4–120 range of the sand and gravel bed tests carried out by Sleath (1987). The oscillation-scale Reynolds number is given by

$$Re = \frac{AU_0}{\nu} \tag{25}$$

where ν the kinematic viscosity. Here, $Re \sim 1.7 \times 10^5$. The roughness Reynolds number is

$$Re_{k_N} = \frac{u_{*m} k_N}{\nu}. \tag{26}$$

Based on the results in Fig. 18 (i.e. using Eq. (18) to determine f_w over the indicated range of $A/k_N = (r_h/A)^{-1}$, $A = 0.52$ m, and $U_0 = 0.33$ m/s), $68 \lesssim Re_{k_N} \lesssim 7700$. The criterion for fully rough turbulent oscillatory flow, corresponding to the friction factor being independent of Re, is $Re_{k_N} > 70$ (Kamphuis, 1975; Schlichting, 1979). This condition is satisfied by the present experiments, except possibly for the initial runs when the bed was nearly flat.

In Fig. 18a, r_h is based on Eq. (19) with $\Lambda = 2.2$, and in panel (b) based on Eq. (22) with $\Gamma = 3$. The dashed lines are the curves predicted via Eq. (18). Agreement with the predicted curve is less good when ripple steepness is included in the hydraulic roughness.

The f_w estimates from the YD246 test are anomalously low during the early runs, as is especially evident in the log-scale plots in Fig. 18: e.g. the cluster of five data points at high values of A/r_h, corresponding to low values of f_w and roughness (recall that A is constant for all the tests). This five-point cluster corresponds to anomalously low values of u_{*m} (Fig. 15a), and to values of σ_η which persisted at low levels after the test was initiated (Fig. 6b). The anomaly appears to be due to the initial state of the bed which, unlike the other two runs, exhibited a slight convex upward profile with ~ 2 mm amplitude, thus contributing ca. 0.14 cm to σ_η. Since elevation variations with 2 mm amplitude and meter-scale wavelengths are unlikely to contribute significantly to the hydraulic roughness, ca. 0.1 cm could justifiably be subtracted from the σ_η values for this five-point cluster. Such a reduction in σ_η would bring the associated points into closer agreement with the predicted curves in Fig. 18.

5. Discussion

5.1. Commentary on the stress estimation methods

For any one of the three methods, the estimates of u_{*m} exhibit a dependence on σ_η which is highly consistent, i.e. independent of PFIR type, and of single-frequency vs. dual-frequency operation and, for the most part, highly repeatable among three independent trials (Figs. 15 and 16). The estimates differ systematically among the three methods, however, and this warrants some discussion.

The law-of-the-wall analysis, as implemented here, is based on the velocity profile segment extending upward from the maximum bed elevation, plus the additional 5 mm offset to avoid contamination of the slant-beam velocities by the bottom return. Thus, this velocity profile segment is located in the outer, lower shear, region of the boundary layer, which is displaced progressively upward as the ripples grow. Consequently, the peak stress lags the maximum Kart speed (Fig. 14b), and the estimates of bottom stress are likely to be biased low. The estimates are also unreliable when the bed is nearly flat initially, as indicated in Fig. 16.

Unlike the velocity profiles used in the law-of-the-wall fits, the Reynolds stress profiles extend to within 5 mm of the *local* bed level, and therefore the maximum observed stress can occur closer to the bed than the maximum bed elevation, in some cases being located within the ripple troughs as in Fig. 13a. The Reynolds stress profiles are noisy however, which is to be expected given that only 13 cycles are included in the phase averages here. (LDA measurements indicate that 50 cycles are required for stable estimates of second order statistics in turbulent oscillatory boundary layers Sleath, 1987; Jensen, 1988). Thirteen-cycle runs were used here because the ripples could undergo significant evolution on time scales longer than a few minutes (Figs. 6 and 8). Partly to reduce the noise, the phase-averaged Reynolds stresses were further averaged in 0.1 s intervals. The choice of averaging interval was a compromise between noise reduction and minimizing the bed elevation change during the interval. Thus, in seeking the maximum value in a noisy signal, it is likely that the Reynolds stress estimates are biased high. Nevertheless, as the data in Fig. 13a and b indicate, the

estimates are embedded in high stress zones of like sign, and are therefore representative in that sense.

Thus, the Reynolds stress as determined here provides an upper bound on the maximum phase-averaged stress, and the law-of-the-wall provides a lower bound. The defect stress estimates lie between these bounds. For this reason, and also because the defect stress method yielded the best estimates of bottom stress for fixed gravel beds (Hay et al., 2012b), the defect stress estimates were used here for the comparisons to the empirical relations for f_w and r_h. While these comparisons are encouraging in our view, it is important to emphasize that the estimates are based on extrapolating the acceleration defect integral. The contribution made by the extrapolation to the stress estimate is not insignificant, increasing from 20% to 40% over the observed range of σ_η. Also, the most appropriate choice for the lower limit of integration is uncertain. This limit was taken here to be the average bed level, because this level would remain relatively constant (i.e. independent of ripple height) as the ripples evolved.

5.2. Comparison to fixed roughness results

The present law-of-the-wall and Reynolds stress results contrast sharply with our measurements over fixed gravel roughness, for which the peak near-bed Reynolds stresses were systematically lower, and the log law estimates systematically larger, than the defect stress: by a factor of ~ 3, and by 50%, respectively (Hay et al., 2012b). There are differences in the analyses, necessitated by the relative non-uniformity of the spatial distribution of the geometric roughness of ripples compared to gravel. Notably, the averaging interval for the Reynolds stress estimates for gravel was 0.5 s, compared to 0.1 s here. Also, as mentioned previously, z_0 was fixed at $2.5D_{50}$ for the log law estimates from the gravel data, but was necessarily a free parameter here. However, it is also the case that the maximum value of the roughness Reynolds number, Re_{k_N}, in the fixed gravel trials was $\lesssim 500$, more than an order of magnitude lower than the maximum value of the roughness Reynolds numbers in the present mobile bed experiments. Furthermore, the geometric character of the roughness is very different: compared to ripples, the gravel surface is highly three-dimensional. Thus, on the cm-scales of the MFDop beamwidth, the geometric character of the ripple roughness, together with the higher values of Re_{k_N} and the correspondingly thicker boundary layer, can be expected to enable the turbulent fluctuations contributing to the stress to be better resolved by the MFDop over rippled beds.

5.3. Suspended sediment stratification

Another difference between the gravel and mobile bed experiments is that in the latter case the bed was a source of sediment, which then admits the possibility that the work done against the (negative) buoyancy forces associated with stratification by suspended sediment might have contributed significantly to the observed stress. The MFDop backscatter amplitude was calibrated vs. sand concentration in the particle-laden jet facility described in Hay (1991), using the same sand as in the RippleKart experiments. The phase-averaged concentrations, C, were computed for the points of maximum Reynolds stress in Fig. 13, yielding $C=1.8$ and 8.9 kg/m^3 for the first and second half-cycles, respectively. The associated values of the gradient Richardson number

$$Ri_G = -\frac{g}{\rho}\frac{\partial C}{\partial z}\left[\frac{\partial u_{Lo}}{\partial z}\right]^{-2} \tag{27}$$

are small: 0.005 and 0.07. While the suspended sediment concentrations are less than 1% by volume, their contribution to the combined density of the water/solid mixture is non-negligible (compared to salinity in the coastal ocean, for example). The gradient Richardson numbers remain much less than 1 nonetheless, due to the high shear in the boundary layer.

The possible importance of sediment stratification vis-a-vis the stress estimates presented here is not ruled out by the above values of C and Ri_G. The magnitude of the contribution is a function of flux Richardson number (Monin and Yaglom, 1971): viz.

$$Ri_F = \frac{g}{\rho}\frac{\overline{w'C'}}{\overline{u'w'}\partial u_{Lo}/\partial z} \tag{28}$$

Note that the numerator and denominator can be estimated directly from the MFDop data. The analysis, however, involves a detailed examination of the backscatter amplitudes and the associated estimates of suspended sediment concentration (and size), which is beyond the scope of the present paper.

5.4. Acceleration forces

As Nielsen (1992, p. 7) has pointed out, the acceleration force acting on a particle in an accelerating flow may differ from that for a particle being accelerated through a stationary fluid. The question arises as to whether this effect might produce differences between the shear stresses above the oscillating tray in the RippleKart apparatus and comparable measurements in an oscillatory flow tunnel. For the case in which the particle is being accelerated through the fluid, the force associated with the acceleration is $\rho(s+C_M)V_p\,\mathrm{d}u/\mathrm{d}t$, where ρ is the density of the fluid, s is the specific gravity of the sediment grains, V_p is the particle volume exposed to the flow, and C_M is the added mass coefficient. The ratio between the force associated with the shear stress on the particle and the acceleration force is

$$\frac{u_*^2}{(s+C_M)\omega u_0}\frac{A_p}{V_p} \sim \frac{u_*^2}{(s+C_M)\omega u_0 D} \tag{29}$$

where A_p is the projected area of the particle, and oscillatory motion has been assumed. For the other case in which the flow accelerates past a stationary particle, the ratio takes the same form but with s replaced by unity. For 200 μm diameter sand grains, $s=2.7$ (quartz), $C_M=0.5$ [the value for a sphere: (Lamb, 1945, p. 124)], and $u_0=30$ cm/s, the denominator is 1.2 cm^2/s^2, which is 4–25 times less than the observed values of u_*^2 (Fig. 15a). When account is taken of the 60–70° phase of the maximum shear stress relative to maximum acceleration, this difference is increased by an additional factor of 2–3. Thus, in the present experiments the maximum shear stress on a sand grain at rest on the bed would have been much greater than the acceleration of the grain through the water, and the same would be true in an oscillatory flow tunnel under the same conditions. This is not to say that the effect did not in some way influence the development of the ripples. However, it is likely that other factors (e.g. end effects associated with the finite-length tray) were more important.

The pressure gradient across the grains, equivalent in the boundary layer approximation to the flow acceleration, can also affect the sediment response if its magnitude approaches the grain immersed weight (Sleath, 1994). The ratio of the maximum pressure difference across the grain $\rho\omega u_0 D$ to the immersed weight per unit area is given by $S=\omega u_0/(s-1)g$, which takes the value 0.011 here. Thus, the equivalent pressure gradient force is small compared to the force of gravity, and very much smaller than the ca. 0.3 threshold required for plug flow (Zala Flores and Sleath, 1998). (This result is not unexpected, since plug development is normally associated with higher energy sheet flow conditions.)

5.5. Reference level for the bed shear stress

As discussed in Section 5.1, the acceleration defect integral can be extrapolated to the bed level. The estimates here of the half-cycle maximum stress are ensemble averages in both time (the phase average) and ripple "space" (the replicate experiments). Because the ripples were different in each experiment, the latter is a crude equivalent to a horizontal average (more replicates would be needed to achieve actual equivalence). The most appropriate choice of bed level for the horizontally averaged stress over very rough boundaries is not clear, however, even for uni-directional flow (Nikora et al., 2007). The average bed level has been used here: that is the level that would be midway between ripple crest and trough for geometrically regular ripples, a choice for which laboratory measurements of stress over fixed artificial dunes in uni-directional flow provide a precedent (McLean et al., 1999).

For mobile beds in sheet flow conditions, Nielsen and Guard (2011) have pointed out that the bed level at which to specify the bed shear stress for sediment transport prediction purposes is not well defined. For the O(0.1) Shields parameters in the present experiments, the uncertainty in the choice of bed level associated with moving grains is necessarily on the order of the grain diameter. An additional uncertainty for remote acoustic measurements of boundary layer processes above mobile beds, and one likely to be greater than the grain diameter here at least, is the distinction and non-trivial difference between the acoustic and hydrodynamic bed levels.

6. Summary and conclusions

Results are presented on the vertical structure of flow and stress within oscillatory boundary layers above evolving sand ripples from experiments using a prototype wide-band coherent Doppler profiler, the MFDop. The experiments were carried out in an oscillating boundary facility, the RippleKart, with beds of 0.216 mm median diameter sand, 10 s oscillation period, and 0.9 m excursion. The corresponding value of the Shields parameter was 0.11. The MFDop velocity profiles, each representing the average of 10 consecutive pulse pairs, were acquired with 0.87 mm vertical resolution (in single-frequency mode) and 1.5 mm resolution (dual-frequency) at 85 Hz. The duration of each data run was slightly longer than 13 oscillation periods (i.e. ~ 2 min), and the runs were acquired consecutively. The total elapsed time for each experiment was $\lesssim 50$ min. Three trials were carried out, two with the MFDop operating in dual-frequency mode but with different filters implemented in the digital receiver, and one in single-frequency mode.

The bed evolved from an initially flattened state through 5 cm wavelength, nearly two-dimensional ripples to 12 cm wavelength, three-dimensional ripples. The associated ripple heights increased from ca. 0.2 cm to ca. 1.4 cm on average, while average ripple steepness increased from ca. 0.04 to ca. 0.15. The corresponding values of the roughness Reynolds number ranged from 68 initially to ≤ 7700 at the completion of the test, assuring fully rough turbulent flow in the boundary layer. The time series of RMS bed elevation, σ_η, exhibit the logistic-type behaviour observed by Davis et al. (2004), particularly at the initial transition from nearly flat bed to two-dimensional ripples. The peak of the bed elevation spectrum shifts towards lower spatial frequencies with time as observed by Davis et al. (2004) and, at spatial frequencies well above the peak, the spectra exhibit a saturation range analogous to the saturation range in surface gravity wave spectra.

The velocity magnitude and phase profiles (in the frame of reference moving with the Kart) exhibit the expected velocity overshoot and phase lead in the boundary layer. The boundary layer thickness and maximum phase lead in the boundary layer increase as the ripples grow in height and wavelength. The maximum observed phase leads are $\sim 20^\circ$, comparable to the values obtained in investigations of turbulent oscillatory boundary layers above fixed roughness beds both using Laser Doppler Anemometry (Sleath, 1987; Jensen, 1988) and the MFDop (Hay et al., 2012a).

Bottom stress was estimated via: (1) the Reynolds stress; (2) the vertical integral of the acceleration defect (i.e. the defect stress); and (3) the law-of-the-wall. Values for u_{*m} (the maximum friction velocity in a half-cycle) obtained via the Reynolds stress are larger than the defect stress estimates (by a factor of 2); the best-fit values from the law-of-the-wall are lower than the defect stress estimates, by $\lesssim 50\%$.

Values of the bed friction factor, f_w, computed from the defect stress estimates of u_{*m} and the amplitude of the Kart motion (the latter corrected for the reaction flow in the tank) are compared to predictions based on the relationships proposed by Nielsen (1992) for the hydraulic roughness of (equilibrium) sand ripples in oscillatory flow. Nielsen's compilation of the then available data for mobile sand ripples yielded $r_h = \Lambda\eta_0$ for the hydraulic roughness in low to moderate energy conditions (grain roughness Shields parameters below 0.5), with $1 < \Lambda < 3$. The values of Λ obtained here are in the same range, with a representative value of ~ 2.2, which is towards the upper end of the range reported by Nielsen. However, Nielsen used the empirical relation between f_w and r_h suggested by Swart (1974), whereas the modified form of this relation proposed by Nielsen (based on subsequent measurements) is used here, which accounts for the difference. Nielsen's proposed relation for r_h included the effects of ripple steepness: viz. $r_h = 8\Gamma\eta_0^2/\lambda_0$, with $\Gamma = 1$. Our results do yield a high value for Γ (~ 3) only ca. 50% of which can be accounted for by Nielsen's use of Swart's f_w vs. r_h relation. It is suggested that the remaining 50% can be attributed to the low steepness of the ripples in the present experiments, compared to the ~ 0.2 steepness typical of equilibrium orbital-scale ripples. However, it is important to point out that a value for Γ close to 3 has also been reported by Thorne et al. (2002), based on measurements of the suspended sediment concentration profile above a rippled sand bed. The steepness of their ripples ranged from 0.12 to 0.15, comparable to the values here at longer elapsed times (> 30 min).

Nielsen included a second term to account for the effect of moving sediment grains on the observed roughness: $170D_{50}\sqrt{\theta_{2.5}-0.05}$. Since for a given grain size this term is a function of only the grain roughness Shields parameter, $\theta_{2.5}$, and the critical Shields parameter corresponding to the threshold for grain motion (0.05), it should represent the limiting value of r_h (and therefore f_w) prior to ripple formation. The present data, however, exhibit a trend towards the fixed-grain value of f_w at low values of the geometric ripple roughness (Fig. 17). This result indicates that either: (a) $170D_{50}\sqrt{\theta_{2.5}-0.05}$ overestimates the moving grain contribution to the roughness for the conditions of the present experiments; or (b) the MFDop measurements underestimate the bottom stress during the early stages of ripple development when the geometric roughness is small. With respect to the latter possibility, it is certainly the case that the MFDop profiles of $u(z,t_k)$ capture a smaller fraction of the total contribution to the vertically integrated acceleration defect under such conditions, since the 5 ± 1 mm thickness of the near-bed zone contaminated by the large amplitude bottom return is then a large fraction of the thickness of the oscillatory boundary layer.

Overall, the results from these mobile bed experiments with the prototype MFDop are encouraging. The values of u_{*m} obtained from each of three stress estimation methods are self-consistent and repeatable. The analyses implemented for each of the three

methods are such that the defect stress estimates are expected to be bounded above and below by the Reynolds stress and law-of-the-wall estimates respectively, as observed. The defect stress estimates yield values of f_w and r_h which are in reasonably good agreement with existing empirical formulae.

Future directions include: (a) investigating the effects of suspended sediment stratification on the stress estimates; and (b) exploring the law-of-the-wall and defect stress closer to the bed. This latter possibility is not easily investigated in the context of evolving ripples. A different experiment with equilibrium orbital-scale ripples might be revealing, and would in any case help to interpret estimates of u_* over slowly migrating or stationary ripples in the field.

Finally, the present observed results for the time history of the bed friction factor over evolving ripples are in reasonable agreement with values predicted using empirical formulae based mainly on ripples in equilibrium with the forcing. This agreement suggests that the ripples remained in quasi-equilibrium with the forcing during their development. As the conditions of the experiments (i.e. medium- to fine-grained sand, 10 s oscillation period, O(1) m excursion) are comparable to nearshore and inner shelf conditions during the onset and waning stages of wave-forcing events, the present results tend to support the assumption of quasi-steadiness in models of ripple development under low-to-moderate energy forcing.

Acknowledgments

The authors gratefully acknowledge the contributions of Wesley Paul and Robert Craig to the development of the MFDop signal conditioning hardware and DAQ software, without which the project would not have been possible. This work was funded by grants from the US Office of Naval Research Geosciences Program, and from the Natural Sciences and Engineering Research Council of Canada.

References

Bagnold, R.A., 1946. Motion of waves in shallow water. Interaction between waves and sand bottoms. Proceedings of the Royal Society of London Series A 187, 1–15.

Batchelor, G.K., 1967. An Introduction to Fluid Dynamics. Cambridge University Press, New York.

Betteridge, K.F.E., Bell, P.S., Thorne, P.D., Williams, J.J., 2005. Evaluation of a triple-axis coherent Doppler velocity profiler for measuring near-bed flows: a field study. Journal of Atmospheric and Oceanic Technology 23, 90–106.

Carstens, M.R., Neilsen, F.M., Altinbilek, H.D., 1969. Bedforms generated in the laboratory under oscillatory flow. CERC Tech Memo 38, U.S. Army Corps of Engineers.

Chou, Y.-J., Fringer, O.B., 2010. A model for the simulation of coupled flow-bed form evolution in turbulent flows. Journal of Geophysical Research 115 (C10041). doi:10.1029/2010JC006103.

Christoffersen, J.B., Jonsson, I.G., 1985. Bed friction and dissipation in a combined current and wave motion. Ocean Engineering 12 (5), 387–423.

Clifton, H.E., Dingler, J.R., 1984. Wave-formed structures and paleoenvironmental reconstruction. Marine Geology 60, 165–198.

Crawford, A.M., Hay, A.E., 1998. A simple system for laser-illuminated video imaging of sediment suspension and bed topography. IEEE Journal of Oceanic Engineering 23 (1), 12–19.

Davis, J.P., Walker, D.J., Townsend, M., Young, I.R., 2004. Wave-formed sediment ripples: transient analysis of ripple spectral development. Journal of Geophysical Research 109 (C07020). doi:10.1029/2004JC002307.

Dillon, J., Zedel, L., Hay, A.E., 2011. Automatic tuning of a velocity estimator for pulse-to-pulse coherent Doppler sonar. In: White, J.R., Williams, A.J., III (Eds.), IEEE/OES/CMTC 10th Working Conference on Current, Waves and Turbulence Measurement, pp. 230–236.

Folk, R.L., 1980. Petrology of Sedimentary Rocks. Hemphill Publishing Co.

Foster, D., Beach, R., Holman, R., 2000. Field observations of the wave bottom boundary layer. Journal of Geophysical Research 105, 19,631–19,647.

Fredsoe, J., Deigaard, R., 1992. Mechanics of Coastal Sediment Transport. World Scientific (369pp.).

Grant, W., Madsen, O., 1986. The continental-shelf bottom boundary layer. Annual Review of Fluid Mechanics 18, 265–305.

Hay, A.E., 1991. Sound scattering from a particle-laden turbulent jet. Journal of the Acoustical Society of America 90, 2055–2074.

Hay, A.E., 2011. Geometric bottom roughness and the bed state storm cycle. Journal of Geophysical Research 116 (C04017). doi:10.1029/2010JC006687.

Hay, A.E., Zedel, L., Craig, R., Paul, W., 2008. Multi-frequency pulse-to-pulse coherent Doppler sonar profiler. In: Ninth Working Conference on Current Measurement Technology. IEEE/OES/CMTC, IEEE, Charleston, SC, pp. 25–29.

Hay, A.E., Zedel, L., Cheel, R., Dillon, J., 2012a. Observations of the vertical structure of turbulent oscillatory boundary layers above fixed roughness beds using a prototype wide-band coherent Doppler profiler: 1. The oscillatory component of the flow. Journal of Geophysical Research 117. doi:10.1029/2011JC007113.

Hay, A.E., Zedel, L., Cheel, R., Dillon, J., 2012b. Observations of the vertical structure of turbulent oscillatory boundary layers above fixed roughness beds using a prototype wide-band coherent Doppler profiler: 2. Turbulence and stress. Journal of Geophysical Research 117. doi:10.1029/2011JC007114.

Holleman, I., Beekhuis, H., 2003. Analysis and correction of dual PRF velocity data. Journal of Atmospheric and Oceanic Technology 20, 443–453.

Hurther, D., Lemmin, U., 2001. A correction method for turbulence measurements with a 3D acoustic Doppler velocity profiler. Journal of Atmospheric and Oceanic Technology 18, 446–458.

Hurther, D., Thorne, P.D., Bricault, M., Lemmin, U., Barnoud, J.-M., 2011. A multi-frequency acoustic concentration and velocity profiler (ACVP) for boundary layer measurements of fine-scale flow and sediment transport processes. Coastal Engineering 58, 594–605.

Jensen, B., 1988. Experimental Investigation of Turbulent Oscillatory Boundary Layers. Institute of Hydrodynamics and Hydraulic Engineering, Technical University of Denmark, Lyngby.

Jensen, B., Sumer, B., Fredsoe, J., 1989. Turbulent oscillatory boundary layers at high Reynolds numbers. Journal of Fluid Mechanics 206, 265–297.

Justesen, P., 1988. Turbulent Wave Boundary Layers. Series Paper 43. Technical University of Denmark, Lyngby.

Kamphuis, J.W., 1975. Friction factors under oscillatory waves. Journal of Waterways Harbours Coastal Engineering 101, 135–144.

Lamb, H., 1945. Hydrodynamics, sixth ed. Dover, New York (790pp.).

Lhermitte, R., Lemmin, U., 1994. Open-channel flow and turbulence measurement by high-resolution Doppler sonar. Journal of Atmospheric and Oceanic Technology 11, 1295–1308.

Lofquist, K.E.B., 1986. Drag on naturally rippled beds under oscillatory flows. Misc. Paper CERC-86-13, U.S. Army Corps of Engineers.

Maier, I., Hay, A.E., 2009. Occurrence and orientation of anorbital ripples in nearshore sands. Journal of Geophysical Research 114 (F04022). doi:10.1029/2008JF001126.

Marieu, V., Bonneton, P., Foster, D.L., Ardhuin, F., 2008. Modeling of vortex ripple morphodynamics. Journal of Geophysical Research 113 (C09007). doi:10.1029/2007JC004659.

McLean, S.R., Wolfe, S.R., Nelson, J.M., 1999. Spatially averaged flow over a wavy surface revisited. Journal of Geophysical Research 104, 15,743–15,753.

Monin, A.S., Yaglom, A.M., 1971. Statistical Fluid Mechanics: Mechanics of Turbulence, vol. 1. MIT Press, Cambridge, MA (769pp.).

Nielsen, P., 1981. Dynamics and geometry of wave-generated ripples. Journal of Geophysical Research 86 (C7), 6467–6472.

Nielsen, P., 1992. Coastal Bottom Boundary Layers and Sediment Transport. World Scientific, River Edge, New Jersey (324pp.).

Nielsen, P., Guard, P.A., 2011. Vertical scales and shear stresses in wave boundary layers over movable beds. Proceedings of the International Conference on Coastal Engineering 32 (1).

Nikora, V.I., McLean, S., Coleman, S., Pokrajac, D., McEwan, I., Campbell, L., Aberle, J., Clunie, D., Koll, K., 2007. Double-averaging concept for rough-bed open-channel and overland flows: applications. Journal of Hydraulic Engineering 133 (8), 884–895.

Phillips, O.M., 1966. The Dynamics of the Upper Ocean. Cambridge University Press, London (261pp.).

Raupach, M.R., 1992. Drag partition on rough surfaces. Boundary-Layer Meteorology 60, 375–395.

Rolland, T., Lemmin, U., 1997. A two-component acoustic velocity profiler for use in turbulent open-channel flow. Journal of Hydraulic Research 35 (4), 545–562.

Schlichting, H., 1979. Boundary Layer Theory, seventh ed. McGraw-Hill Inc., New York.

Sleath, J., 1987. Turbulent oscillatory flow over rough beds. Journal of Fluid Mechanics 182, 369–409.

Sleath, J., 1990a. Seabed boundary layers. In: LeMehaute, B., Hanes, D.M. (Eds.), The Sea: Ocean Engineering Science, vol. 9, Pt B. Wiley, pp. 693–727.

Sleath, J., 1990b. Velocity and bed friction in combined flows. In: Proceedings of the 22nd Conference of Coastal Engineering, ASCE, pp. 450–463.

Sleath, J., 1994. Bed load transport in oscillatory flow. In: Belorgey, M., Rajaona, R., Sleath, J. (Eds.), Sediment Transport Mechanisms in Coastal Environments and Rivers. World Scientific, River Edge, NJ, pp. 93–106.

Smith, D., Sleath, J.F.A., 2005. Transient ripples in oscillatory flows. Continental Shelf Research 25, 458–501. doi:10.1016/j.csr.2004.10.012.

Smyth, C., Hay, A.E., Zedel, L., 2002. Coherent Doppler profiler measurements of near-bed suspended sediment fluxes and the influence of bedforms. Journal of Geophysical Research 107 (C8). doi:10.1029/2000JC000760.

Stanton, T.P., 1996. Probing ocean wave boundary layers with a hybrid bistatic/monostatic Coherent Acoustic Doppler Profiler. In: Microstructure Sensors in the Ocean Workshop, Mt. Hood.

Swart, D., 1974. Offshore Sediment Transport and Equilibrium Beach Profiles. Technical Report 131, Delft Hydraulics Lab.
Testik, F.Y., Voropayev, S.I., Fernando, H.J.S., 2005. Adjustment of sand ripples under changing water waves. Physics of Fluids 17 (7), 07214.
Thorne, P.D., Williams, J.J., Davies, A.G., 2002. Suspended sediments under waves measured in a large scale flume facility. Journal of Geophysical Research 107 (C8). doi:10.1029/2001JC000988.
Thornton, E.B., Guza, R.T., 1983. Transformation of wave height distribution. Journal of Geophysical Research 88 (C10), 5925–5938.
Traykovski, P., 2007. Observations of wave orbital scale ripples and a nonequilibrium time-dependent model. Journal of Geophysical Research 112 (C06026). doi:10.1029/2006JC003811.
Traykovski, P., Hay, A.E., Irish, J.D., Lynch, J.F., 1999. Geometry, migration, and evolution of wave orbital ripples at LEO-15. Journal of Geophysical Research 104, 1505–1524.
Trowbridge, J., Agrawal, Y., 1995. Glimpses of a wave boundary layer. Journal of Geophysical Research 100 (C10), 20729–20743.
Wiberg, P.L., Harris, C.K., 1994. Ripple geometry in wave-dominated environments. Journal of Geophysical Research 99 (C1), 775–789.
Zala Flores, N., Sleath, J., 1998. Mobile layer in oscillatory sheet flow. Journal of Geophysical Research 103 (C6), 12783–12793.
Zedel, L., 2008. Modelling pulse-to-pulse coherent Doppler sonar. Journal of Atmospheric and Oceanic Technology 25, 1834–1844.
Zedel, L., Hay, A., 2010. Resolving velocity ambiguity in multi-frequency, pulse-to-pulse coherent Doppler sonar. IEEE Journal of Oceanic Engineering 35 (4), 847–850.
Zrnic, D.S., 1977. Spectral moment estimates from correlated pulse pairs. IEEE Transactions on Aerospace and Electronic Systems 13, 344–354.